RSC Advances

ROYAL SOCIETY OF CHEMISTRY

PAPER

View Article Online
View Journal | View Issue

Cite this: *RSC Adv.*, 2026, **16**, 30158

Theoretical investigation of Rb-based double halide perovskites for photovoltaic, photocatalytic water splitting, and CO_2 reduction applications

Rifat Rafiu,[a] Imtiaz Ahamed Apon,[b] Md. Azizur Rahman,*[c] Amnah Mohammed Alsuhaibani,[d] Moamen S. Refat,[e] Mohamed Benghanem,*[f] S. AlFaify[g] and Noureddine Elboughdiri[h]

Received 4th April 2026
Accepted 19th May 2026

DOI: 10.1039/d6ra02841a

rsc.li/rsc-advances

Understanding the intrinsic properties of emerging materials is essential for advancing next-generation optoelectronic and energy-related technologies, and DFT offers an effective route for this purpose. In this work, the structural, electronic, optical, photocatalytic, and photovoltaic properties of lead-free Rb_2NaRhX_6 (X = F, Cl, Br, I) double halide perovskites are systematically investigated using a combined DFT and SCAPS-1D simulation approach. Structural analysis confirms that all compounds crystallize in stable cubic phases and satisfy thermodynamic, mechanical, and dynamical stability criteria through negative formation energies, Born stability conditions, and the absence of imaginary phonon frequencies. Electronic band-structure calculations including PBE, spin–orbit coupling (SOC) and HSE06 hybrid functional corrections reveal direct band-gap semiconducting behavior with a systematic reduction in band gap from fluoride to iodide compositions. Optical analysis demonstrates a pronounced red shift in the absorption edge and enhanced visible-light absorption for the Br- and I-based compounds, indicating strong potential for solar-energy harvesting. Band-edge alignment calculations further show that Rb_2NaRhF_6, $Rb_2NaRhCl_6$, and $Rb_2NaRhBr_6$ possess suitable conduction- and valence-band positions for photocatalytic water splitting, while all investigated compounds exhibit favorable conduction-band potentials for photocatalytic CO_2 reduction reactions. In addition, pH-dependent band-edge analysis suggests stable redox capability across a broad pH range, particularly for the fluoride and chloride systems. Photovoltaic performance was evaluated using an FTO/SnS_2/Rb_2NaRhX_6/Au device architecture in SCAPS-1D, where halide substitution strongly influences carrier transport and device efficiency. Among the studied absorbers, $Rb_2NaRhCl_6$ exhibits the best overall photovoltaic performance, achieving a power conversion efficiency (PCE) of 27.03% with an open-circuit voltage (V_{OC}) of 0.893 V, a short-circuit current density (J_{SC}) of 35.41 mA cm^{-2}, and a fill factor (FF) of 83.56%. These findings establish Rb_2NaRhX_6 double perovskites as promising multifunctional materials for photovoltaic devices, photocatalytic hydrogen production, and CO_2 reduction applications.

1 Introduction

Perovskite solar cells (PSCs) have emerged as one of the most promising next-generation photovoltaic technologies because of their excellent light-harvesting capability, tunable band gap, long carrier diffusion length, and low-cost fabrication potential.[1–3] Despite these advantages, the large-scale application of conventional Pb-based perovskites remains limited by the toxicity of lead and their poor chemical stability.[4,5] These concerns have encouraged extensive research into lead-free and structurally stable alternatives for photovoltaic applications.[6] Among the various candidates, lead-free halide double perovskites and vacancy-ordered derivatives have attracted considerable attention because of their compositional flexibility, reduced toxicity, and promising optoelectronic properties. In-based double perovskites have been widely discussed as

---

[a] *Department of Material Science and Engineering, Khulna University of Engineering & Technology (KUET), Khulna-9203, Bangladesh*

[b] *Electronics and Information Technology, University of South Wales, Treforest, Pontypridd, CF37 1DL, UK*

[c] *Department of Electrical and Electronic Engineering, Begum Rokeya University, Rangpur 5400, Bangladesh. E-mail: azizurrahmanatik49@gmail.com*

[d] *Department of Sports Health, College of Sport Sciences & Physical Activity, Princess Nourah bint Abdulrahman University, P. O. Box 84428, Riyadh 11671, Saudi Arabia*

[e] *Department of Chemistry, College of Science, Taif University, P. O. Box 11099, Taif 21944, Saudi Arabia*

[f] *Physics Department, Faculty of Science, Islamic University of Madinah, Madinah 42351, Saudi Arabia. E-mail: mbenghanem@iu.edu.sa*

[g] *Department of Physics, College of Sciences, King Khalid University, P. O. Box 960, AlQura'a, Abha 61421, Saudi Arabia*

[h] *Chemical Engineering Department, College of Engineering, University of Ha'il, P. O. Box 2440, 81441 Ha'il, Saudi Arabia*

potential absorber materials. Xiao *et al.* critically examined $Cs_2InBiCl_6$ and $Cs_2InSbCl_6$ and showed that, although these materials were initially considered attractive because of their direct band gaps and low effective masses, they are intrinsically unstable due to the oxidation of In(I) to In(III). Their study clearly demonstrated that redox stability must be carefully considered when assessing the practical feasibility of such compounds.[7]

Even with this limitation, $Cs_2InSbCl_6$ has remained an interesting material because of its defect-sensitive electronic and optical behavior. Magaji *et al.* investigated Au substitution at the In site in $Cs_2InSbCl_6$ and reported that the pristine compound possesses a direct band gap of 0.99 eV, while Au incorporation increases the band gap to 1.25 eV.[8] They also found that the doped system exhibits enhanced absorption, reduced reflectivity, and improved optical conductivity, indicating its potential for solar-energy conversion applications. In another study, explored the influence of indium vacancy defects in the same compound and showed that the pristine material behaves as a direct-gap semiconductor, whereas the introduction of an In vacancy drives the system toward metallic character because of electronic-state overlap near the Fermi level.[9] Their results further confirmed that defect formation strongly affects the absorption, reflectivity, and conductivity of $Cs_2InSbCl_6$. These findings suggest that point defects play a decisive role in determining the suitability of this material for photovoltaic applications.[10] Beyond $Cs_2InSbCl_6$, many other lead-free double perovskites have been proposed and analyzed through a combination of first-principles calculations and device simulation. Hossain *et al.* demonstrated that Cs_2BiAgI_6-based solar cells can be significantly improved through transport-layer engineering using DFT, SCAPS-1D, and wxAMPS analyses.[11] Allahyar *et al.* reported a band gap of 1.654 eV for $Cs_2AgBiBr_6$ and predicted a power conversion efficiency of 23.5% for an optimized FTO/AZnO/$Cs_2AgBiBr_6$/CNTS/Au architecture.[12] Uddin *et al.* also highlighted the photovoltaic promise of $Cs_2AgBiBr_6$ through combined DFT and SCAPS-1D investigation.[13] Other lead-free absorbers have likewise shown strong theoretical performance. Lunge *et al.* examined $Cs_2AuBiCl_6$ and reported a band gap near 1.09 eV with optimized efficiencies reaching 21.16% depending on the transport-layer combination.[14] Hossain *et al.* studied Cs_2TiBr_6 and found a direct band gap of 1.534 eV, while their optimized device achieved a PCE of 24.82%.[15] Shivesh *et al.* further improved the simulated efficiency of Cs_2TiBr_6-based solar cells to 29.13% by selecting La-doped $BaSnO_3$ as the ETL and $CuSbS_2$ as the HTL.[16] Similarly, Rehman *et al.* reported that Cs_2TiI_6-based devices can reach a PCE of 28.07%, confirming the promise of Ti-based lead-free double halide perovskites for photovoltaic use.[17] Vacancy-ordered and mixed-halide lead-free perovskites have also been actively explored. Rezini *et al.* investigated $Cs_2SnI_{6-x}Br_x$ alloys and showed that halide substitution effectively tunes the band gap and improves simulated solar-cell efficiency after optimization.[18] Aggarwal *et al.* proposed a machine-learning-guided design for Cs_2SnBr_6-based solar cells and predicted an exceptionally high efficiency of 38.70%, although such values still require experimental confirmation.[19] Porwal *et al.* demonstrated that defect engineering in Cs_2SnI_6 can significantly enhance device efficiency.[20] Amjad *et al.* reported that vacancy-ordered Cs_2PtI_6 can achieve a PCE of 23.52% in an FTO/SnO_2/Cs_2PtI_6/MoO_3/C configuration,[21] while Tariq *et al.* identified Cs_2PdBr_6 as another promising lead-free absorber with an optimized efficiency of 26.00%.[22] More recently, the design of lead-free perovskite solar cells has advanced beyond simple material screening toward integrated strategies that combine electronic-structure calculations, device simulation, and data-driven optimization. Sabbah *et al.* modeled hydrogenated $Cs_2AgBiBr_6$ double perovskite solar cells and reported an efficiency of 26.3% after structural optimization.[23] Neupane *et al.* demonstrated that dual-ETL engineering in $Cs_2AgBi_{0.75}Sb_{0.25}Br_6$-based devices can produce a PCE of 22.11%.[24] Raj *et al.* combined DFT, SCAPS-1D, and machine learning to study $Cs_2CuSbCl_6$, reporting a PCE of 31.50% together with strong humidity-dependent degradation behavior.[25] These studies indicate that the development of environmentally friendly PSCs is increasingly relying on multiscale design approaches that link intrinsic material properties with device architecture and operational stability.

Beyond photovoltaic applications, recent work has also highlighted the strong potential of lead-free double perovskites in photocatalysis and solar fuel generation. For example, first-principles investigations of Cs_2SnGeX_6 (X = Cl, Br, I) demonstrate that these materials combine structural stability with direct band gaps and strong optical absorption, while their band edge positions are suitably aligned for photocatalytic hydrogen production and CO_2 reduction.[26] Similarly, Cs_2TlInX_6 compounds have been shown to satisfy the thermodynamic requirements for overall water splitting, particularly for the Cl and Br-based systems, which exhibit band gaps in the visible-light range and favorable valence and conduction band positions.[27] In addition, studies on hydride-based double perovskites such as Rb_2AlXH_6 (X = In, Tl) reveal that these materials not only support photocatalytic water splitting but also exhibit measurable hydrogen storage capacities, indicating a dual functionality in hydrogen production and storage.[28] Vacancy-ordered systems such as Cs_2OsX_6 further extend this functionality, where band alignment analysis suggests that Cl- and Br-based compounds are suitable for water oxidation, while iodide variants show potential for CO_2 reduction.[29]

In this study, Rb_2NaRhX_6 (X = F, Cl, Br, I) lead-free double halide perovskites are investigated for sustainable solar-energy applications. This material system is selected because the Rb-based A-site cation provides a suitable ionic size for structural stability, while the ordered Na–Rh B-site configuration and Rh d-halogen p hybridization enable tunable electronic properties across the halide series. The structural stability of perovskites is commonly evaluated using the Goldschmidt tolerance factor and octahedral factor, which depend on ionic radii and determine lattice distortion and phase stability.[30] The Rb_2NaRhX_6 composition satisfies these criteria, supporting stable cubic structures. Although many studies have focused on Cs-based lead-free perovskites, systematic investigations of Rb-based Rh-containing double perovskites remain limited. In particular, a comprehensive study covering the full halide series (F–I) and simultaneously linking electronic, optical, photocatalytic, and photovoltaic properties is still lacking. In this context, this work establishes composition–property relationships through combined DFT and SCAPS-1D analysis. To the best of our knowledge, such an integrated investigation of Rb_2NaRhX_6 has not been reported. The results provide guidance for designing stable, lead-free perovskites for solar cells and photocatalytic applications such as water splitting and CO_2 reduction.

2 Computational method

2.1. CASTEP (Cambridge serial total energy package)

The first-principles calculations for Rb_2NaRhX_6 (X = F, Cl, Br, I) double perovskites, belonging to the $A_2BB''X_6$ family, were carried out using the CASTEP module implemented in Material Studio 2023.[31,32] The initial crystallographic information files (CIFs) of Rb_2NaRhX_6 (X = F, Cl, Br, I) were obtained from the Materials Project database and subsequently imported into Material Studio for structural visualization and simulation. According to the Materials Project data, all compounds crystallize in the cubic crystal system with space group $Fm\bar{3}m$ (no. 225) and point group $m\bar{3}m$. The lattice parameters satisfy $\alpha = \beta = \gamma = 90°$ and $a = b = c$, with optimized lattice constants of 6.229 Å for Rb_2NaRhF_6, 7.313 Å for $Rb_2NaRhCl_6$, 7.750 Å for $Rb_2NaRhBr_6$, and 8.378 Å for Rb_2NaRhI_6. The atomic arrangement consists of Rh atoms occupying the 4a (0, 0, 0) Wyckoff position, Na atoms at 4b (1/2, 1/2, 1/2), Rb atoms at 8c (1/4, 1/4, 1/4), and halogen atoms X (X = F, Cl, Br, I) located at the 24e (x, 0, 0) sites, as illustrated in the left panel of Fig. 1.[33] It should be noted that the Na atom occupies the 4b Wyckoff site, which is symmetry-equivalent to (1/2, 1/2, 1/2) in the conventional $Fm\bar{3}m$ setting; however, the coordinate (1/2, 0, 0) used here follows the Materials Project (mp-14038) representation. The optimized structures retained their cubic symmetry without any significant lattice distortion, confirming the structural stability of the compounds.[34] Before evaluating the electronic and optical properties, all structures were fully geometrically optimized to obtain the equilibrium ground-state configurations. The optimization was performed within the framework of density functional theory using the generalized gradient approximation (GGA) and the Perdew–Burke–Ernzerhof (PBE) exchange–correlation functional. A plane-wave cutoff energy of 517 eV, OTFG ultrasoft pseudopotentials, and the Koelling–Harmon relativistic treatment were employed. The self-consistent field convergence tolerance was set to 2.0×10^{-6} eV per atom, with a maximum of 1000 SCF cycles, and a 6 × 6 × 6 Monkhorst–Pack k-point mesh was used during structural optimization. After optimization, the electronic properties were investigated through the calculation of the band structure, total density of states (DOS), and partial density of states (PDOS). The band dispersion was analyzed along the high-symmetry Brillouin-zone path W–L–Γ–X–W–K, where the corresponding k-point coordinates are W (0.500, 0.250, 0.750), L (0.500, 0.500, 0.500), Γ (0.000, 0.000, 0.000), X (0.500, 0.000, 0.500), and K (0.375, 0.375, 0.750). To improve the accuracy of the electronic structure, spin–orbit coupling (SOC) effects were included due to the presence of heavy elements, and the band gap was further refined using the hybrid Heyd–Scuseria–Ernzerhof functional, which is known to provide more reliable band gap estimations compared to standard GGA-PBE. The mechanical stability of the studied compounds was evaluated through the calculation of elastic constants, while dynamical stability was further confirmed by phonon dispersion analysis using the finite displacement method. Using the geometrically optimized structures, the optical properties were further analyzed from the complex dielectric function, from which the absorption coefficient, refractive index, reflectivity, and optical conductivity were derived to evaluate the optoelectronic potential of the studied compounds.

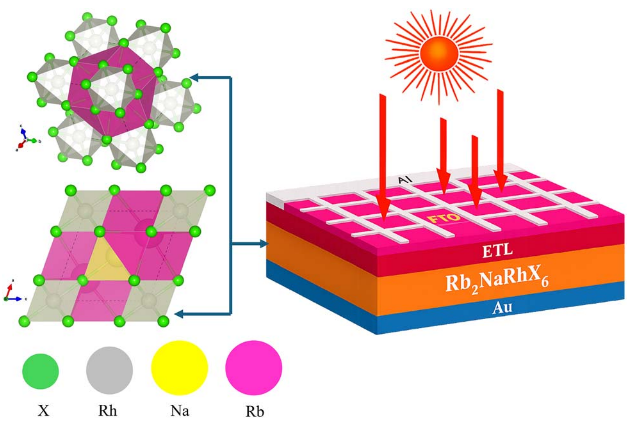

Fig. 1 Optimized crystal structure and device architecture of Rb_2NaRhX_6 (X = F, Cl, Br, I) double perovskites.

2.2. SCAPS-1D

SCAPS-1D simulation is a one-dimensional numerical technique employed to evaluate the photovoltaic potential of Rb_2NaRhX_6 (X = F, Cl, Br, and I) compounds for solar-cell applications. SCAPS-1D, developed at Ghent University, Belgium, simulates device performance by solving Poisson's equation, the continuity equations, and carrier transport equations throughout the different layers of the solar cell illustrated in Fig. 1. This computational approach is important because it enables the prediction of photovoltaic behavior and the optimization of parameters such as layer thickness, doping concentration, defect density, interface properties, and temperature effects. The simulation provides valuable insight into charge-carrier dynamics, band alignment, recombination losses, and power conversion efficiency, thereby helping to identify the most promising Rb-based lead-free perovskite absorbers before experimental fabrication.[35]

The mathematical framework used to analyze the Rb_2NaRhX_6 based solar cell is found on two principal formulations: the Poisson equation (eqn (1)) and the continuity equations for electrons and holes (eqn (2) and (3)). The Poisson equation describes the relationship between the electric field, $E(x)$, dielectric permittivity, and the net charge density within the device. In parallel, the continuity equations account for the transport, generation, and recombination of charge carriers, thereby providing a complete description of carrier dynamics in the photovoltaic system.[36,37]

$$\frac{\mathrm{d}}{\mathrm{d}x}\left(-\varepsilon(x)\frac{\mathrm{d}\psi}{\mathrm{d}x}\right)=q[\{p(x)+N_{\mathrm{D}}{}^{+}(x)\}-\{n(x)+N_{\mathrm{A}}{}^{-}(x)\}] \quad (1)$$

here, $\varepsilon(x)$ denotes the dielectric permittivity, q the electronic charge, $n(x)$ and $p(x)$ the concentrations of electrons and holes, and $N_{\mathrm{D}}{}^{+}(x)$ and $N_{\mathrm{A}}{}^{-}(x)$ represent ionized donor and acceptor densities, respectively.

The continuity equations for holes (eqn (2)) and electrons (eqn (3)) are expressed as,[38]

$$\frac{\partial p}{\partial t}=\frac{1}{q}\frac{\partial j_{\mathrm{p}}}{\partial x}-R_{\mathrm{p}}+G \quad (2)$$

$$\frac{\partial n}{\partial t}=-\frac{1}{q}\frac{\partial j_{\mathrm{n}}}{\partial x}-R_{\mathrm{n}}+G \quad (3)$$

where R_{p} and R_{n} denote the recombination rates of holes and electrons, respectively, and G represents the photogeneration rate. The total current density is given by,

$$J=j_{\mathrm{p}}+j_{\mathrm{n}} \quad (4)$$

The drift–diffusion current densities for holes and electrons are defined as,

$$J_{\mathrm{p}}=q\mu_{\mathrm{p}}pE+qD_{\mathrm{p}}\frac{\mathrm{d}p}{\mathrm{d}x} \quad (5)$$

$$J_{\mathrm{n}}=q\mu_{\mathrm{n}}nE+qD_{\mathrm{n}}\frac{\mathrm{d}n}{\mathrm{d}x} \quad (6)$$

where μ_{p} and μ_{n} are the mobilities of holes and electrons, while D_{p} and D_{n} are their respective diffusion coefficients.

The diffusion length of charge carriers, which correlates with their lifetime and diffusivity, is expressed as,

$$L_{(\mathrm{n,p})}=\sqrt{\tau_{(\mathrm{n,p})}D_{(\mathrm{n,p})}} \quad (7)$$

where τ(n, p) is the carrier lifetime and D(n, p) the diffusion coefficient. Furthermore, the optical absorption within the perovskite layer is modeled in SCAPS-1D using the Tauc relation,

$$\alpha(\lambda)=(A+B/h\nu)\sqrt{h\nu-E_{\mathrm{g}}} \quad (8)$$

here, A and B are material-dependent constants, E_{g} is the bandgap, and h_{v} is the photon energy. This relation provides the absorption coefficient $\alpha(\lambda)$, thereby connecting incident photons with the optical response of the perovskite absorber.

The program calculates key performance parameters such as open-circuit voltage (V_{OC}),[39]

$$V_{\mathrm{OC}}=\frac{n\times k\times T}{q}\ln\left(\frac{I_{\mathrm{ph}}}{I_{\mathrm{O}}}+1\right) \quad (9)$$

Short-circuit current density (J_{SC}),

$$J_{\mathrm{SC}}=q\times A\times G\times\eta \quad (10)$$

Fill factor (FF),[40]

$$\mathrm{FF}=\frac{P_{\mathrm{Max}}}{P_{\mathrm{in}}}=\frac{I_{\mathrm{Max}}\times V_{\mathrm{Max}}}{V_{\mathrm{OC}}\times I_{\mathrm{SC}}} \quad (11)$$

Power conversion efficiency (PCE),[41]

$$\mathrm{PCE}=\frac{I_{\mathrm{SC}}\times\mathrm{FF}\times V_{\mathrm{OC}}}{P_{\mathrm{in}}} \quad (12)$$

The photovoltaic characteristics of $\mathrm{Rb_2NaRhX_6}$ (X = F, Cl, Br, and I) were assessed through the calculation of key device parameters, including the open-circuit voltage (V_{OC}, eqn (9)), short-circuit current density (J_{SC}, eqn (10)), fill factor (FF, eqn (11)), and power conversion efficiency (PCE, eqn (12)). As shown in Fig. 1, the optimized crystal structure and device architecture of $\mathrm{Rb_2NaRhX_6}$ provide the structural and simulation framework for evaluating the solar-cell performance of these materials. Here, P_{in} denotes the incident solar power, n is the diode ideality factor, k is Boltzmann's constant,[42] T is the temperature, I_{ph} is the photo-generated current, I_0 is the reverse saturation current, A represents the active area, G is the irradiance, and η is the quantum efficiency. Incorporating relevant material parameters, such as band gap, electron affinity, dielectric constant, and carrier mobility, enables a comprehensive evaluation of carrier transport, recombination pathways, and defect tolerance in the Rb-based double perovskites.

This combined theoretical approach using CASTEP-based DFT and SCAPS-1D was selected because it enables a direct link between intrinsic material properties and device-level performance. The DFT method implemented in CASTEP, based on a plane-wave pseudopotential framework, is well suited for accurately describing periodic solid-state systems and has been widely validated for calculating the electronic structure and optical properties of halide perovskites. In contrast, SCAPS-1D is specifically designed for thin-film photovoltaic devices and solves the Poisson and carrier continuity equations to simulate charge transport, recombination, and interface effects. Compared to other standalone approaches, this combination provides a more comprehensive evaluation by integrating material-level insights with realistic device modeling. Therefore, this methodology offers an effective and computationally efficient strategy for predicting the photovoltaic potential of lead-free $\mathrm{Rb_2NaRhX_6}$ materials prior to experimental fabrication.

3 Results & discussion

3.1. Structural stability analysis

Structural stability describes whether a crystal is energetically favorable, mechanically robust, and dynamically stable, typically assessed *via* lattice constants, formation energy, elastic constants, and phonon dispersion. Materials are stable when $\Delta E_{\mathrm{f}} < 0$, elastic constants satisfy the Born criteria, and no imaginary phonon frequencies are present. In this section, the materials' stability considering these criteria were highlighted.

Fig. 2 presents the variation of optimized lattice constant, formation energy, and Goldschmidt tolerance factor for

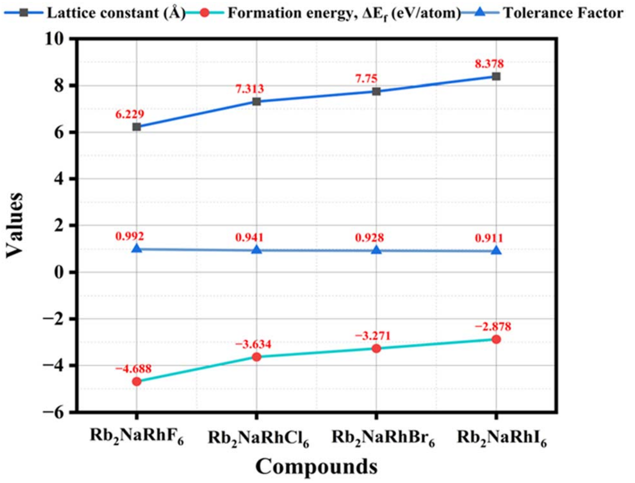

Fig. 2 Variation of lattice constant, formation energy, and tolerance factor for Rb_2NaRhX_6 (X = F, Cl, Br, I) compounds.

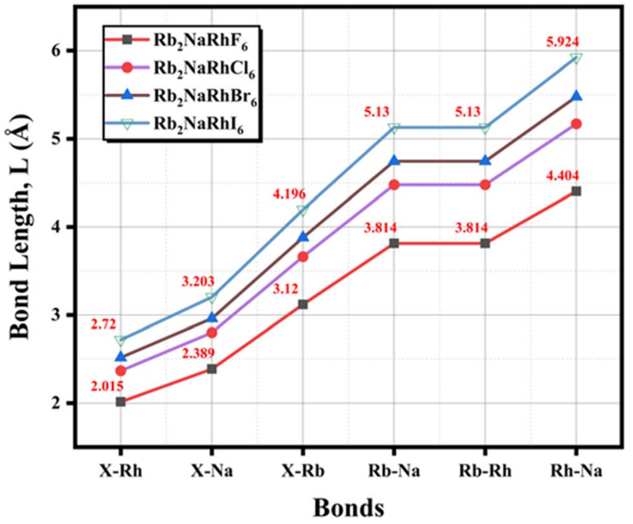

Fig. 3 Variation of bond length of different bonds for Rb_2NaRhX_6 (X = F, Cl, Br, I) compounds.

Table 1 Calculated elastic constants of Rb_2NaRhX_6 (X = F, Cl, Br, I) compounds

Elastic constants	Rb_2NaRhF_6	$Rb_2NaRhCl_6$	$Rb_2NaRhBr_6$	Rb_2NaRhI_6
C_{11} (GPa)	16.391	33.547	24.355	18.762
C_{12} (GPa)	6.995	9.740	4.918	4.537
C_{44} (GPa)	10.313	10.501	6.538	3.648

Rb_2NaRhX_6 (X = F, Cl, Br, I). The lattice constant increases systematically from 6.229 Å (F) to 8.378 Å (I). This trend follows the increase in ionic radius from F^- to I^-, which expands the RhX_6 octahedra and enlarges the unit cell. The formation energy of these compounds was calculated using eqn (1),

$$\Delta E_f = E_{tot}(Rb_2NaRhX_6) - 2E(Rb) - E(Na) - E(Rh) - 6E(X) \tag{13}$$

The formation energy becomes progressively less negative, changing from −4.688 eV per atom (F) to −2.878 eV per atom (I). All values remain negative, indicating that each compound is thermodynamically stable, although stability decreases for heavier halides due to weaker bonding interactions associated with longer bond lengths. Tolerance factor is an indicator for a compound's cubic structure stability expressed as;[43]

$$t = \frac{r_{Rb} + r_X}{\sqrt{2}\left(\frac{r_{Na} + r_{Rh}}{2} + r_X\right)} \tag{14}$$

The Goldschmidt tolerance factor decreases from 0.992 to 0.911 across the series, remaining within the range typical for stable perovskite structures (0.8–1.0). This reduction suggests a gradual increase in structural distortion with increasing halide size, while preserving overall structural integrity.

Fig. 3 shows the variation of bond lengths for different atomic pairs in Rb_2NaRhX_6 compounds. All bond lengths increase consistently from F to I, reflecting the increasing ionic radius of the halide ions. For example, the Rh–X bond length increases from approximately 2.015 Å (F) to about 2.72 Å (I). Similar trends are observed for X–Na and X–Rb interactions, as well as cation–cation separations such as Rb–Na and Rh–Na. This uniform expansion indicates that the crystal lattice accommodates larger halide ions by increasing interatomic distances. The increase in bond length reduces orbital overlap and weakens bonding interactions, which is consistent with the observed decrease in formation energy and elastic stiffness. Overall, the bond length trends confirm the structural expansion and progressive softening of the lattice across the halide series.

The calculated elastic constants (C_{11}, C_{12}, and C_{44}) for the Rb_2NaRhX_6 compounds are listed in Table 1. All elastic constants are positive, and the Born stability criteria for cubic crystals ($C_{11} > 0$, $C_{44} > 0$, $C_{11} - C_{12} > 0$, and $C_{11} + 2C_{12} > 0$) are satisfied for each compound, confirming their mechanical stability. Among the series, $Rb_2NaRhCl_6$ exhibits the highest C_{11} value (33.547 GPa), indicating the greatest resistance to longitudinal deformation. In contrast, Rb_2NaRhI_6 shows the lowest C_{44} value (3.648 GPa), suggesting reduced tendency to shear deformation and a comparatively softer lattice. The general decrease in elastic constants from lighter to heavier halides indicates a reduction in mechanical rigidity, which correlates with increasing bond lengths and weaker interatomic interactions.

Fig. 4 presents the phonon dispersion relations along high-symmetry directions for all four compounds.

The phonon spectra do not exhibit any imaginary (negative) frequencies across the Brillouin zone. This absence of soft modes confirms that all structures are dynamically stable and do not undergo spontaneous lattice distortions. The phonon branches for heavier halides (Br and I) appear at lower frequencies compared to those for F and Cl, reflecting reduced

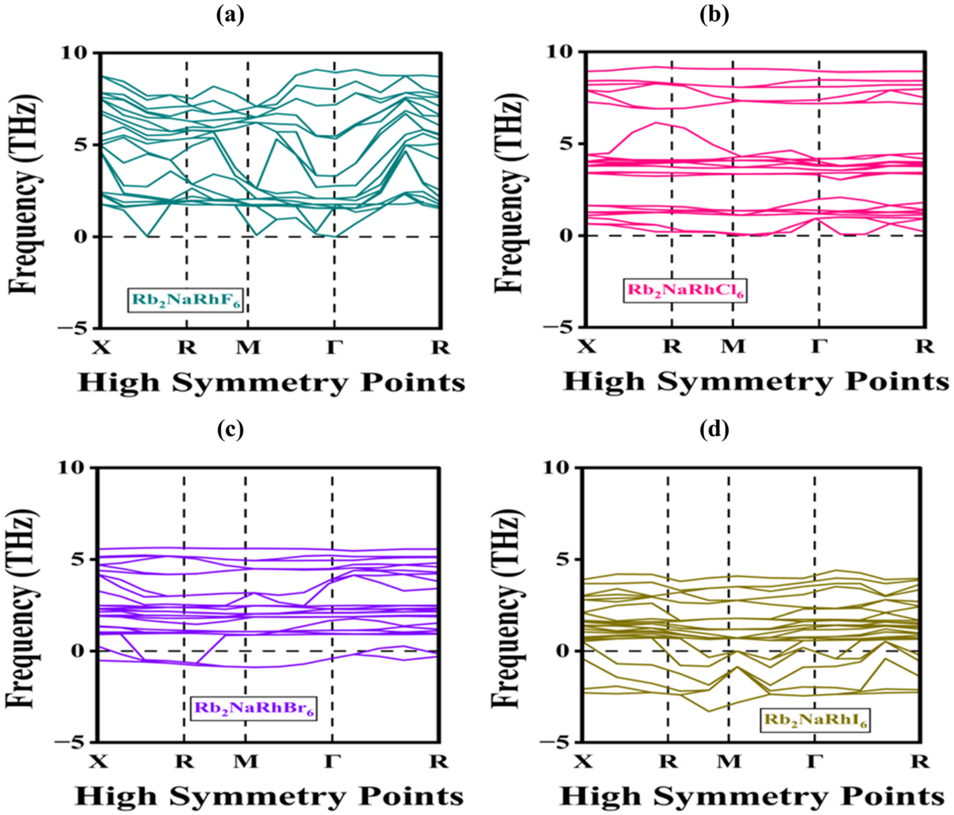

Fig. 4 Phonon dispersion analysis of (a) Rb_2NaRhF_6, (b) $Rb_2NaRhCl_6$, (c) $Rb_2NaRhBr_6$, and (d) Rb_2NaRhI_6 compounds.

force constants and softer lattice vibrations. This trend is consistent with the observed decrease in elastic constants and increase in bond lengths. Overall, the phonon analysis supports the conclusion that all Rb_2NaRhX_6 compounds are dynamically stable, with a gradual reduction in lattice stiffness from F to I.

3.2. Electronic properties

3.2.1. Band structure. The variation of electron energy with crystal momentum in a periodic solid is determined by its electronic band structure. It defines key parameters such as the valence band maximum (VBM), conduction band minimum, and band gap.[44] Calculating the band structure is important for these Rb-based halide compounds to know whether they are a semiconductor, metal, or insulator. As shown in Fig. 5a–d, all investigated compounds exhibit finite band gaps, confirming their semiconducting nature. The electronic band structures were calculated using GGA-PBE, including spin–orbit coupling (SOC), and further corrected using the hybrid HSE06 functional, as shown in Fig. 5a–d. At the PBE level, the band gaps are 1.819 eV (Rb_2NaRhF_6), 1.254 eV ($Rb_2NaRhCl_6$), 0.935 eV ($Rb_2NaRhBr_6$), and 0.594 eV (Rb_2NaRhI_6). Upon inclusion of SOC, the band gaps decrease to 1.702 eV, 1.135 eV, 0.816 eV, and 0.460 eV, respectively, indicating a significant relativistic effect, particularly for the heavier Br- and I-based compounds. The HSE06 functional yields larger band gaps of 4.769 eV, 3.198 eV, 2.659 eV, and 1.649 eV for Rb_2NaRhF_6, $Rb_2NaRhCl_6$, $Rb_2NaRhBr_6$, and Rb_2NaRhI_6, respectively, providing a more accurate estimation of the fundamental band gap. The strong reduction of the band gap under SOC, especially for $Rb_2NaRhBr_6$ and Rb_2NaRhI_6, highlights the importance of relativistic effects in these systems and indicates that PBE values alone are insufficient for quantitative predictions.

Moreover, all compounds exhibit a direct band gap, as both the CBM and VBM are located at or very close to the *X*-point. This direct transition is advantageous for efficient optical absorption and emission, making these materials promising candidates for optoelectronic applications. The conduction bands display greater dispersion compared to the valence bands, indicating a lower effective mass of electrons and suggesting enhanced electron mobility. Based on the calculated band gap values, the F- and Cl-based compounds are more suitable for visible-light optoelectronic applications and photovoltaic devices, with $Rb_2NaRhCl_6$ having a band gap close to the optimal range for solar energy conversion. In contrast, the Br- and I-based compounds, with narrower band gaps, are more appropriate for infrared detection and low-energy optoelectronic applications.

3.2.2. Total density of states (TDOS). Total density of states is another measure that gives a prediction on the number of available electronic states at each energy level and is derived from the band structure. To identify the band gap, locate the Fermi level, and understand how electrons contribute to transport and optical properties can be predicted from calculating the TDOS. The plot of TDOS, as shown in Fig. 6, gives

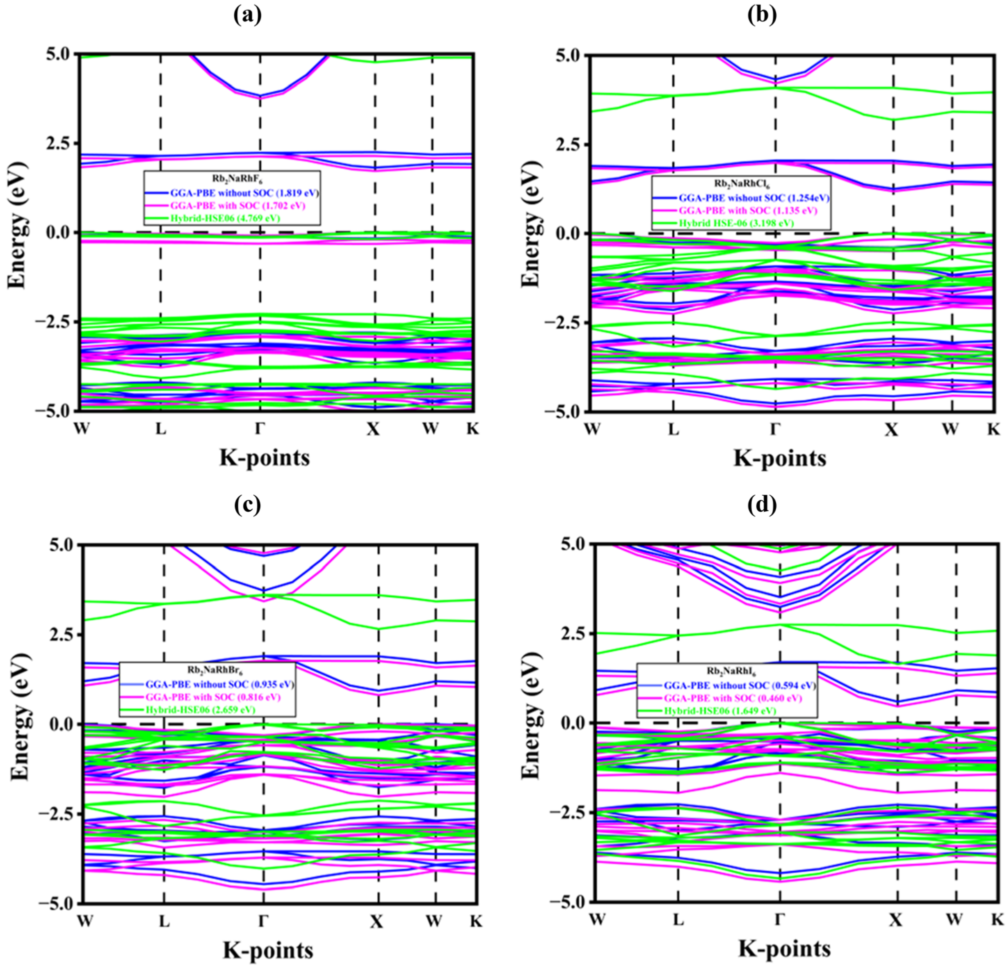

Fig. 5 Band structure of (a) Rb_2NaRhF_6, (b) $Rb_2NaRhCl_6$, (c) $Rb_2NaRhBr_6$, and (d) Rb_2NaRhI_6 double perovskite materials.

a useful insight into their semiconducting behavior. The band gap decreased from F to I, as seen by the narrowing gap between the valence and conduction regions. The valence band (−6 to 0 eV) shows strong peaks, indicating dense occupied states.

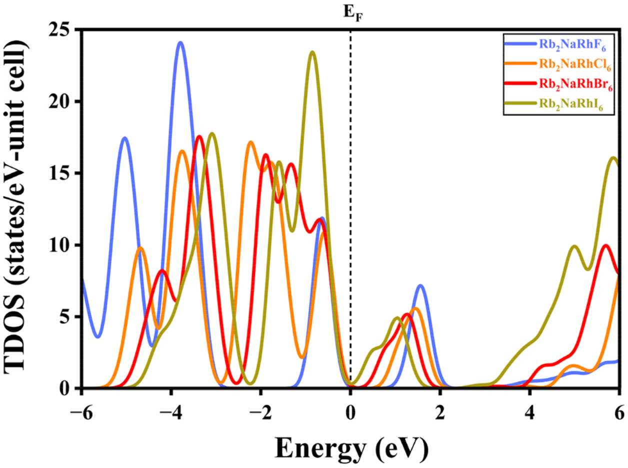

Fig. 6 Total density of states of double perovskite Rb_2NaRhX_6 (X = F, Cl, Br, I) double perovskite materials.

Similarly, the conduction band has fewer states that shift close to the Fermi level from F to I, suggesting the electronic excitation. These features arise from orbital hybridization, mainly between Rh d and halogen p orbitals. As the halogen changes from F to I, the p orbitals become more extended, increasing p–d hybridization and shifting energy levels, which reduces the band gap. This trend explains the tunable electronic and optical properties of these compounds.

3.3. Optical behavior analysis

Analysis of optical properties is essential to evaluate how materials interact with electromagnetic radiation and their potential for light-harvesting applications. Parameters such as the absorption coefficient, optical conductivity, and dielectric function provide insight into electronic transitions, energy absorption, and charge response under illumination. These properties therefore help determine the suitability of Rb_2NaRhX_6 (X = F, Cl, Br, I) compounds for photocatalytic and photovoltaic applications.

The optical absorption properties of Rb_2NaRhX_6 (X = F, Cl, Br, and I) were analyzed to evaluate their suitability for photocatalytic and photovoltaic applications, as illustrated in Fig. 7a.

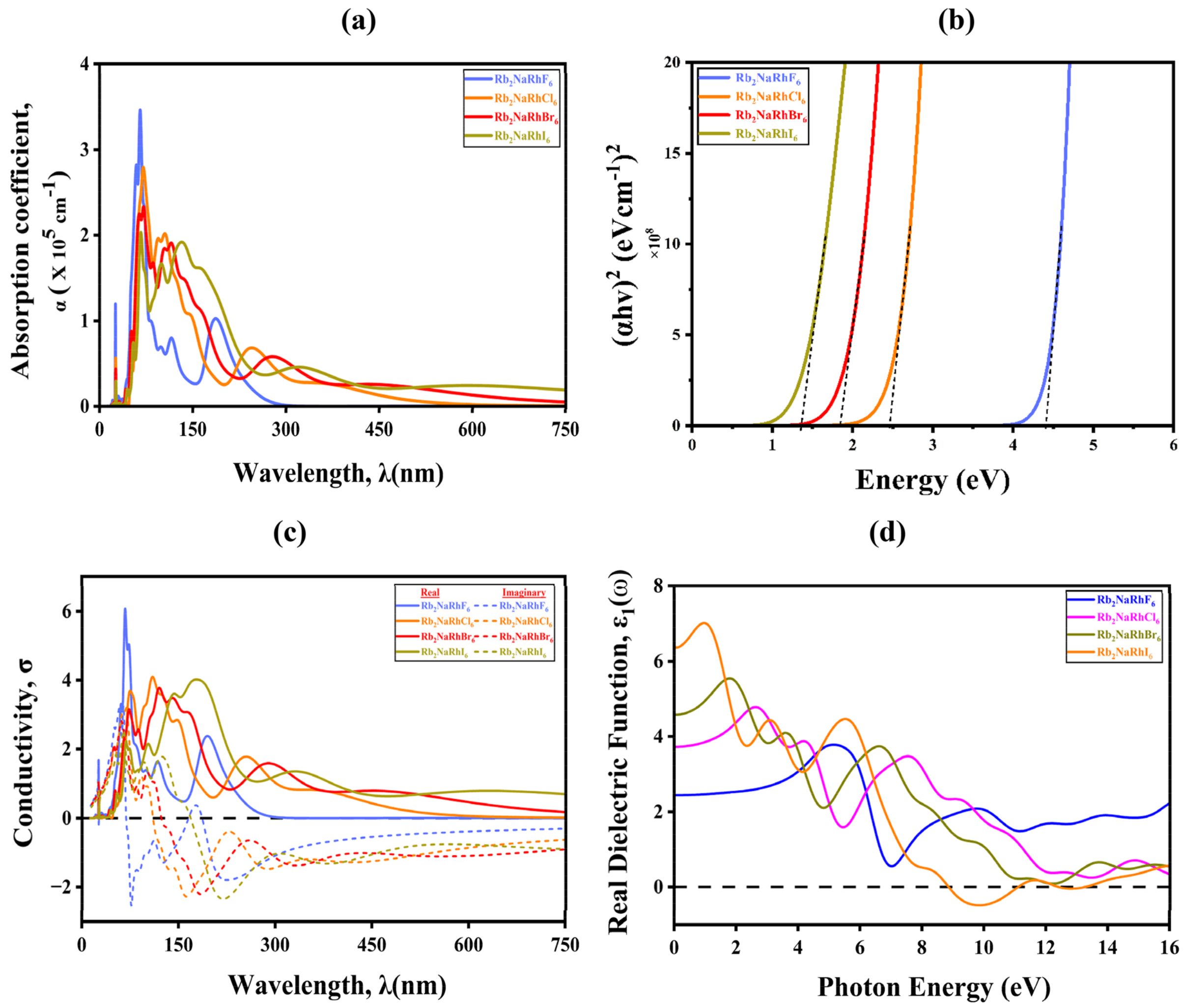

Fig. 7 Calculated optical characteristics of Rb_2NaRhX_6 (X = F, Cl, Br, and I), showing (a) wavelength-dependent absorption spectra and (b) Tauc plots used to estimate the optical band gap, (c) real and imaginary optical conductivity (d) real dielectric function.

The absorption coefficient (α), which measures the probability of photon absorption and subsequent electron–hole pair generation, is a key parameter governing light-harvesting efficiency.[42–44] All compounds exhibit strong absorption in the ultraviolet region, with a systematic red shift in the absorption edge from Rb_2NaRhF_6 to Rb_2NaRhI_6. The absorption onset occurs at approximately 90 to 100 nm for Rb_2NaRhF_6, ~120 nm for $Rb_2NaRhCl_6$, ~150 nm for $Rb_2NaRhBr_6$, and ~180 to 200 nm for Rb_2NaRhI_6, while the maximum absorption coefficients reach $\sim 3.4 \times 10^5$ cm^{-1}, 2.7×10^5 cm^{-1}, 2.3×10^5 cm^{-1}, and 2.0×10^5 cm^{-1}, respectively. Notably, $Rb_2NaRhBr_6$ and Rb_2NaRhI_6 exhibit extended absorption tails toward longer wavelengths, indicating improved interaction with the solar spectrum, whereas Rb_2NaRhF_6 shows negligible visible-light absorption. To further analyze the optical band gap E_g was determined using Tauc's relation, given by eqn (15). The graph of $(\alpha h\nu)^n$ as a function of energy $h\nu$ is shown in Fig. 7b, which allows us to extract the optical band gap values from the absorption spectra. This provides crucial insights into the material's potential for photovoltaic and photocatalytic applications.[45]

$$(\alpha h\nu)^n = A(h\nu - E_g) \tag{15}$$

where α is the absorption coefficient, $h\nu$ is the photon energy, A is a proportionality constant, and E_g is the band gap, with the exponent of $n = 2$ indicating the direct allowed transition and $n = 1/2$ indirect transition.

The optical band gaps obtained from the Tauc plots in Fig. 7b are 4.406 eV (Rb_2NaRhF_6), 2.466 eV ($Rb_2NaRhCl_6$), 1.850 eV ($Rb_2NaRhBr_6$), and 1.373 eV (Rb_2NaRhI_6), showing a systematic decrease with increasing halide size. This reduction is consistent with enhanced orbital hybridization and the progressive narrowing of the band gap. From an application perspective, the wide band gap of Rb_2NaRhF_6 restricts its activity to ultraviolet-driven processes, while $Rb_2NaRhCl_6$ shows only limited visible-light utilization. In contrast, $Rb_2NaRhBr_6$ falls within the optimal band gap range for visible-light photocatalysis, allowing efficient absorption and charge generation under solar irradiation. Rb_2NaRhI_6, with a narrower band gap of 1.373 eV, is particularly suitable for photovoltaic applications due to its strong overlap with the solar spectrum, although it's very small band gap may increase carrier recombination and reduce oxidation capability in photocatalytic processes.

It should be noted that the electronic band gap obtained from band-structure calculations and the optical band gap extracted from Tauc analysis are related but not necessarily identical quantities. The electronic band gap corresponds to the energy separation between the valence-band maximum and conduction-band minimum, whereas the optical band gap is associated with optically allowed electronic transitions and the absorption behavior of the material. In complex halide double perovskites, noticeable differences between electronic and optical band gaps have also been reported previously. For example, $Cs_2SnGeCl_6$, $Cs_2SnGeBr_6$, and Cs_2SnGeI_6 were reported to exhibit electronic band gaps of 1.40, 0.88, and 0.59 eV, while their corresponding optical band gaps were 2.19, 1.86, and 1.55 eV, respectively.[46] Similar behavior has also been reported for $K_2ScCuBr_6$ double perovskite systems.[47] Such variations may arise from transition-selection rules, weak low-energy absorption transitions, excitonic effects, and the nature of optical absorption processes. Based on the calculated band gap range and absorption behavior, $Rb_2NaRhBr_6$ appears to offer the most balanced performance for visible-light-driven photocatalytic applications, whereas Rb_2NaRhI_6 is more suitable for solar-energy-conversion and photovoltaic applications.

Optical conductivity (σ) describes how charge carriers respond to incident light and reflects photon-induced electronic transitions.[48,49] It includes a real part associated with energy absorption and charge carrier generation, and an imaginary part related to polarization effects. This property is closely linked to the dielectric function and absorption behavior of materials. For solar cell applications, high optical conductivity indicates efficient conversion of light into mobile charge carriers. Materials with strong and broad conductivity in the visible region are particularly desirable for enhanced solar energy utilization. As shown in Fig. 7c, the real part of the optical conductivity for Rb_2NaRhX_6 compounds begins to rise sharply in the ultraviolet region, consistent with the absorption observed in Fig. 7a. The onset of $\sigma_1(\omega)$ occurs at approximately 90–100 nm for Rb_2NaRhF_6, 120 nm for $Rb_2NaRhCl_6$, 150 nm for $Rb_2NaRhBr_6$, and 180–200 nm for Rb_2NaRhI_6. The maximum real optical conductivity is observed at around 110 nm for Rb_2NaRhF_6 with a peak value exceeding 6 (arb. units), indicating the strongest interband transition among the studied compounds. For $Rb_2NaRhCl_6$, the peak occurs near 130 nm with a value of approximately 4, while $Rb_2NaRhBr_6$ shows a peak around 140 to 150 nm with a magnitude close to 3.5. In contrast, Rb_2NaRhI_6 exhibits a broader and slightly shifted peak centered near 160 nm with a maximum value around 4, indicating more extended but less intense transitions. The imaginary part of the optical conductivity shows corresponding negative peaks in similar wavelength ranges, confirming strong electronic polarization and transition activity. Notably, as the halide changes from F to I, the conductivity spectra shift toward longer wavelengths, reflecting band gap narrowing and enhanced electronic delocalization. From an application perspective, Rb_2NaRhF_6 shows the highest conductivity but is limited to the ultraviolet region, reducing its solar relevance. In contrast, $Rb_2NaRhBr_6$ and Rb_2NaRhI_6 extend toward longer wavelengths, with Rb_2NaRhI_6 offering the most favorable visible-light response.

Table 2 Highest absorption coefficient and dielectric starting value of Rb_2NaRhX_6 (X= F, Cl, Br, I)

Compound	Highest absorption coefficient, α (cm^{-1})	Dielectric starting value (F/m)
Rb_2NaRhF_6	3.46×10^5	2.443
$Rb_2NaRhCl_6$	2.764×10^5	3.722
$Rb_2NaRhBr_6$	2.313×10^5	4.577
Rb_2NaRhI_6	1.992×10^5	6.398

Dielectric function is a fundamental optical property that demonstrates how a material responds to an external electromagnetic field. It consists of real and imaginary parts; among them, the real part illustrates the material ability to store energy through polarizations, and the imaginary one responds to absorption. The graph presented in Fig. 7d shows the plotted real dielectric function for Rb_2NaRhX_6 compounds with a photon energy ranging from 0 to 16 eV. As shown in Table 2, at zero photon energy, the dielectric constants were approximately 2.443 for Rb_2NaRhF_6, 3.722 for $Rb_2NaRhCl_6$, 4.577 for $Rb_2NaRhBr_6$, and 6.398 for Rb_2NaRhI_6, showing a systematic increase with heavier halides due to enhanced polarizability. As energy increases, the $\varepsilon_1(\omega)$ exhibits peaks corresponding to interband electronic transitions. The highest values observed for Rn_2NaRhI_6 (7.0 at 1 eV), $Rb_2NaRhBr_6$ (5.5 at 1.95 eV), $Rb_2NaRhCl_6$ (4.72 around 2 to 3 eV), and Rb_2NaRhF_6 (~3.7 near ~5 eV). Beyond these peaks, the dielectric function decreases, and in the case of the I-based compound, $\varepsilon_1(\omega)$ becomes negative around 9 to 11 eV, indicating a plasma-like reflective behavior. Thus, from the comparative plot, the Rb_2NaRhI_6 has the largest dielectric function, followed by the Br, Cl, and F, consistent with increasing orbital size and stronger electronic polarization.

4 Photocatalytic applications

Photocatalytic processes, including water splitting and carbon dioxide (CO_2) reduction, have received considerable attention because they offer a route for converting solar energy into chemical fuels.[50] In particular, photocatalytic water splitting enables the production of hydrogen (H_2), which is considered a clean and renewable energy carrier.[51] Similarly, photocatalytic CO_2 reduction provides a pathway for converting greenhouse gases into valuable fuels and chemicals such as CO, CH_4, and CH_3OH under light irradiation. These processes require semiconductor materials with appropriate band gap energies and suitable band edge positions relative to the redox potential of the targeted reactions.

As illustrated in Fig. 8, the photocatalytic mechanism begins with the absorption of incident light by the Rb_2NaRhX_6 (X = F, Cl, Br, and I) double perovskites, generating electron–hole (e^-/h^+) pairs through excitation across the band gap (E_g). The photogenerated electrons are promoted to the conduction band (C_B), while holes remain in the valence band (V_B). These charge carriers then migrate to the surface, where they participate in

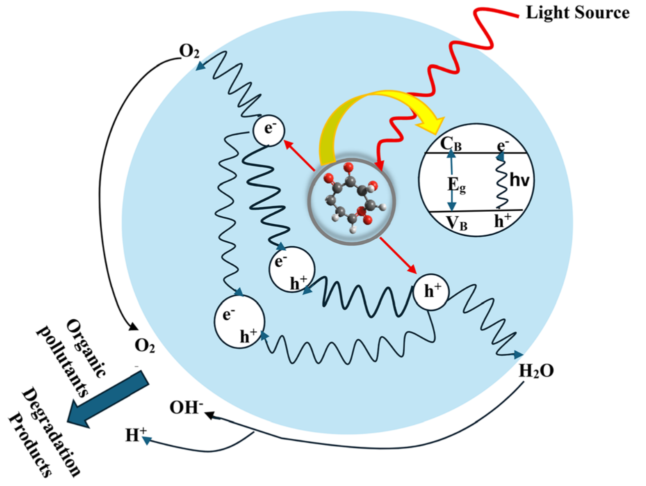

Fig. 8 A schematic diagram describing the photocatalytic water splitting process.

redox reactions. The conduction band electrons reduce adsorbed species (*e.g.*, H^+ to H_2 or CO_2 to reduced carbon products), while the valence band holes oxidize water molecules to produce O_2 and reactive intermediates such as OH radicals. To evaluate the photocatalytic efficiency, the positions of the conduction band minimum (CBM) and valence band maximum (VBM) are aligned with respect to the normal hydrogen electrode (NHE). This alignment determines whether the band edges straddle the redox potentials required for hydrogen evolution reaction (HER) and oxygen evolution reaction (OER), as well as possible CO_2 reduction pathways.

4.1. Hydrogen production

Photocatalytic water splitting is an environmentally sustainable method for producing hydrogen (H_2) using solar energy. In this process, semiconductor photocatalysts absorb photons and generate electron–hole pairs that drive reduction and oxidation reactions at the catalyst surface.[52] The overall reaction proceeds through two half-reactions:

$$2H^+ + 2e^- \rightarrow H_2 \tag{16}$$

$$2H_2O \rightarrow O_2 + 4H^+ + 4e^- \tag{16.1}$$

$$2H_2O \rightarrow 2H_2 + O_2 \tag{16.2}$$

For efficient water splitting, the photocatalyst must possess appropriate band gap energy and band edge alignment relative to the redox potential of water. The conduction band minimum (CBM) must lie at a potential more negative than the hydrogen reduction level (0 eV *vs.* NHE), while the valence band maximum (VBM) must lie at a potential more positive than the oxygen evolution level (+1.23 eV *vs.* NHE).[53]

The band edge potentials of the Rb_2NaRhX_6 (X = F, Cl, Br, I) compounds were estimated using the electronegativity approach according to the following relations:[49–51]

Table 3 Comparison of optical band gap, CBM, VBM, and dielectric peak values of Rb_2NaRhX_6 (X = F, Cl, Br, I)

Compound	Optical band gap, E_g (eV)	CBM (eV)	VBM (eV)
Rb_2NaRhF_6	4.406	−0.503	3.903
$Rb_2NaRhCl_6$	2.466	−0.322	2.144
$Rb_2NaRhBr_6$	1.850	−0.293	1.557
Rb_2NaRhI_6	1.373	−0.401	0.972

$$E_{CBM} = \chi - E_0 - \frac{E_g}{2} \tag{17}$$

$$E_{VBM} = \chi - E_0 + \frac{E_g}{2} \tag{18}$$

where E_0 is the free-electron energy on the hydrogen scale (4.5 eV), E_g is the band gap energy of the compound, and χ is the absolute electronegativity of the semiconductor.[54–56] It should be noted that the Mulliken electronegativity approach provides only a qualitative estimation of band edge positions, with typical uncertainties on the order of ∼0.3–0.5 eV. Therefore, the calculated CBM and VBM values are interpreted as indicative trends rather than quantitatively precise energy levels.[54–56]

The absolute electronegativity of the Rb_2NaRhX_6 compounds can be estimated using the geometric mean of the electronegativities of the constituent atoms,[57]

$$\chi_{Rb_2NaRhX_6} = \left(\chi_{Rb}{}^{2}\chi_{Na}\chi_{Rh}\chi_{X}{}^{6}\right)^{1/10} \tag{19}$$

While this method is widely used for initial screening of photocatalytic materials, it does not explicitly account for surface effects, electrostatic potential alignment, or many-body interactions, which can significantly influence the absolute band edge positions. The calculated band edge potentials for the investigated compounds are summarized in Table 3. The calculated results indicate that the CBM of all Rb_2NaRhX_6 compounds lies below the hydrogen reduction potential (0 eV *vs.* NHE), suggesting that photogenerated electrons can efficiently reduce protons to produce hydrogen. However, the ability to oxidize water depends on the position of the valence

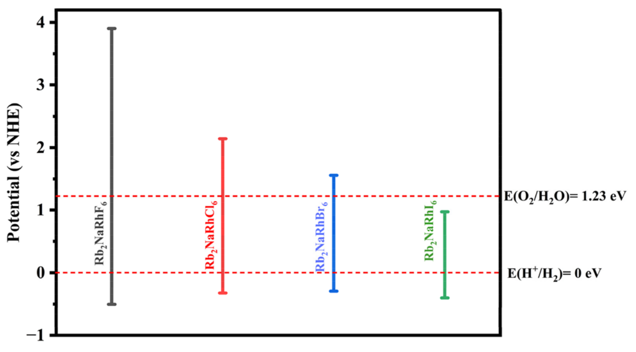

Fig. 9 Photocatalytic band edge potentials of Rb_2NaRhX_6 (X = F, Cl, Br, I) relative to the normal hydrogen electrode (NHE).

band relative to the oxygen evolution potential (+1.23 eV *vs.* NHE).[58]

As shown in Fig. 9 among the studied materials, Rb_2NaRhF_6, $Rb_2NaRhCl_6$, and $Rb_2NaRhBr_6$ exhibit valence band maximum (VBM) values higher than the oxygen evolution potential (1.23 eV *vs.* NHE), suggesting favorable thermodynamic alignment for photocatalytic water splitting. Specifically, the VBM positions are approximately 3.903 eV for Rb_2NaRhF_6, 2.144 eV for $Rb_2NaRhCl_6$, and 1.557 eV for $Rb_2NaRhBr_6$, all of which lie above the oxidation potential of water. Their conduction band minima (CBM) are located around −0.503 eV, −0.322 eV, and −0.293 eV, respectively, which are above the hydrogen evolution potential (0 eV), suggesting that these materials possess suitable band edge alignment for both oxygen and hydrogen evolution reactions.

In contrast, Rb_2NaRhI_6 shows a VBM value of approximately 0.972 eV, which lies slightly below the water oxidation potential (1.23 eV). This indicates that it may not effectively drive the oxygen evolution reaction. However, its CBM is positioned near −0.401 eV, which remains above the hydrogen reduction potential, suggesting that it can still facilitate hydrogen production.

The photocatalytic behavior is also affected by the pH of the reaction medium. The band edge potentials shift with pH according to the following relations,[59]

$$E_{\mathrm{CBM}}^{\mathrm{pH}} = E_{\mathrm{CBM}}^{\mathrm{pH}=0} - 0.05911 \times \mathrm{pH} \tag{20}$$

$$E_{\mathrm{VBM}}^{\mathrm{pH}} = E_{\mathrm{VBM}}^{\mathrm{pH}=0} - 0.05911 \times \mathrm{pH} \tag{21}$$

As shown in Fig. 10a and b, increasing the pH causes both the valence band maximum (VBM) and conduction band minimum (CBM) to shift toward lower potentials in an approximately linear manner across the pH range from 0 to 14. In Fig. 10a, the VBM of Rb_2NaRhF_6 decreases from about 3.9 eV at pH 0 to approximately 3.1 eV at pH 14. Similarly, $Rb_2NaRhCl_6$ shows a reduction from roughly 2.1 eV to 1.35 eV, while $Rb_2NaRhBr_6$ decreases from about 1.5 eV to 0.75 eV over the same pH range.

The Rb_2NaRhI_6 compound exhibits the lowest VBM values, declining from approximately 0.9 eV at pH 0 to nearly 0.15 eV at pH 14. A comparable trend is observed for the conduction band edges in Fig. 10b. The CBM of Rb_2NaRhF_6 shifts from around −0.55 eV at pH 0 to about −1.30 eV at pH 14. For $Rb_2NaRhCl_6$, the CBM decreases from approximately −0.40 eV to −1.15 eV, while $Rb_2NaRhBr_6$ shifts from about −0.35 eV to −1.10 eV. In the case of Rb_2NaRhI_6, the CBM moves from roughly −0.48 eV at pH 0 to about −1.22 eV at pH 14. These results indicate that the downward shift of the band edges with increasing pH reduces the oxidation capability of the photocatalysts under strongly alkaline conditions, as the VBM gradually approaches lower potential. Nevertheless, Rb_2NaRhF_6 maintains relatively high VBM values across the entire pH range, indicating stable oxidation capability and favorable redox alignment. In contrast, the chloride and bromide variants exhibit a moderate reduction in oxidation ability at higher pH values. Overall, the band alignment analysis in Fig. 10a and b suggests that Rb_2NaRhF_6, $Rb_2NaRhCl_6$, and $Rb_2NaRhBr_6$ remain promising candidates for photocatalytic hydrogen production, whereas Rb_2NaRhI_6 primarily supports hydrogen evolution and may be less suitable for complete water splitting. The band-edge positions were estimated using the Mulliken electronegativity approach, which provides a first-order description of the relative alignment of conduction and valence bands. This method does not explicitly account for surface effects, catalytic active sites, overpotentials, or charge-carrier recombination processes. Consequently, the present analysis focuses on bulk thermodynamic alignment, while detailed photocatalytic performance requires additional investigation including surface reaction pathways and kinetic effects.

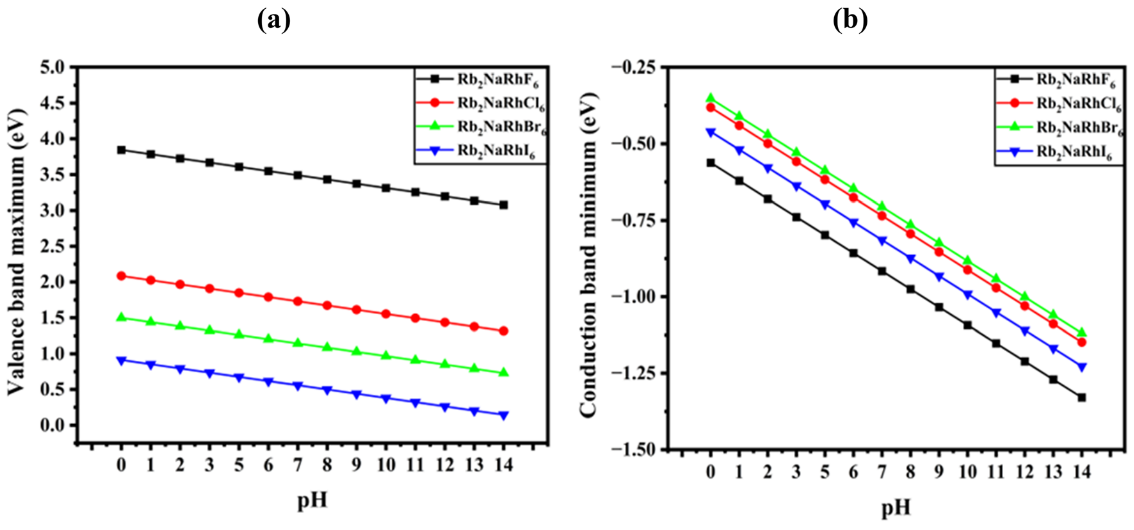

Fig. 10 pH-dependent variation of (a) valence band maximum (VBM) and (b) conduction band minimum (CBM) for Rb_2NaRhX_6 (X = F, Cl, Br, and I) compounds.

4.2. CO_2 photo-degradation capacity

Photocatalytic reduction of carbon dioxide (CO_2) is an attractive strategy for mitigating greenhouse gas emissions while producing valuable fuels and chemical intermediates.[60] In this process, semiconductor photocatalysts utilize solar energy to convert CO_2 into useful products such as methane (CH_4), methanol (CH_3OH), formic acid (HCOOH), and carbon monoxide (CO). The main photocatalytic CO_2 reduction reactions can be expressed as,

$$CO_2 + 8H^+ + 8e^- \rightarrow CH_4 + 2H_2O \tag{22}$$

$$CO_2 + 2H^+ + 2e^- \rightarrow HCOOH \tag{22.1}$$

$$CO_2 + 2H^+ + 2e^- \rightarrow CO + H_2O \tag{22.2}$$

$$CO_2 + 6H^+ + 6e^- \rightarrow CH_3OH + H_2O \tag{22.3}$$

For these reactions to be thermodynamically feasible, the conduction band potential of the photocatalyst must be sufficiently negative to transfer electrons to the CO_2 molecules, while the valence band potential must be positive enough to drive oxidation reactions that supply the necessary protons.

Fig. 11 compares the band edge potentials of the Rb_2NaRhX_6 (X = F, Cl, Br, I) compounds with the standard CO_2 reduction potentials referenced to the normal hydrogen electrode (NHE). The dashed reference lines indicate the reduction potentials for CO_2/CH_4 (0.169 eV), CO_2/CH_3OH (0.017 eV), CO_2/CO (−0.53 eV), and $CO_2/HCOOH$ (−0.19 eV). The calculated conduction band minimum (CBM) positions of the Rb_2NaRhX_6 compounds lie above several of these CO_2 reduction potentials, indicating that these materials can provide thermodynamic driving force for CO_2 reduction reactions at the level of bulk band alignment. As illustrated in Fig. 11, the CBM values are approximately −0.55 eV for Rb_2NaRhF_6, −0.40 eV for $Rb_2NaRhCl_6$, −0.35 eV for $Rb_2NaRhBr_6$, and −0.48 eV for Rb_2NaRhI_6. These positions are sufficiently negative to drive the formation of products such as HCOOH (−0.19 eV) and CO (−0.53 eV), indicating that the materials exhibit sufficient reducing potential for several CO_2 reduction pathways at the bulk electronic level. In addition, Rb_2NaRhF_6 and $Rb_2NaRhCl_6$ exhibit relatively high valence band maximum (VBM) potentials, which enhance the oxidation capability required to balance the reduction reactions during photocatalysis. This band alignment is favorable for coupled reduction and oxidation processes based on bulk electronic structure. Halide substitution strongly influences the photocatalytic properties of the Rb_2NaRhX_6 series. As the halogen changes from F → Cl → Br → I, the valence band shifts toward lower potentials, which reduces the oxidation capability of the photocatalyst. This trend modifies the relative band positions and may influence carrier dynamics. Consequently, Rb_2NaRhF_6 exhibits the most favorable band alignment relative to the CO_2 reduction potentials shown in Fig. 11, followed by $Rb_2NaRhCl_6$ and $Rb_2NaRhBr_6$, whereas Rb_2NaRhI_6 displays comparatively weaker oxidation potential. Overall, the band edge alignment presented in Fig. 11 indicates that the Rb_2NaRhX_6 double perovskites possess suitable electronic structures for photocatalytic CO_2 reduction under visible-light irradiation. Among them, Rb_2NaRhF_6 demonstrates the most suitable combination of conduction and valence band positions, suggesting superior potential for efficient CO_2 conversion and solar fuel production. However, it should be noted that favorable band-edge alignment alone is not sufficient to fully establish efficient CO_2 photoreduction performance and product selectivity. In practical photocatalytic systems, several additional factors, including the adsorption behavior of CO_2 molecules, surface active sites, reaction kinetics, charge-transfer characteristics, and carrier recombination dynamics, significantly influence the overall photocatalytic efficiency. Moreover, the formation and stability of multi-electron reaction intermediates (such as COOH, CO, and H species) play critical roles in determining the selectivity toward specific reduction products. Therefore, although the present band-edge analysis confirms the thermodynamic feasibility of CO_2 reduction for the Rb_2NaRhX_6 compounds, further investigations involving surface-reaction analysis, adsorption-energy calculations, and carrier-dynamics studies are necessary to comprehensively evaluate the photocatalytic mechanism and catalytic selectivity.

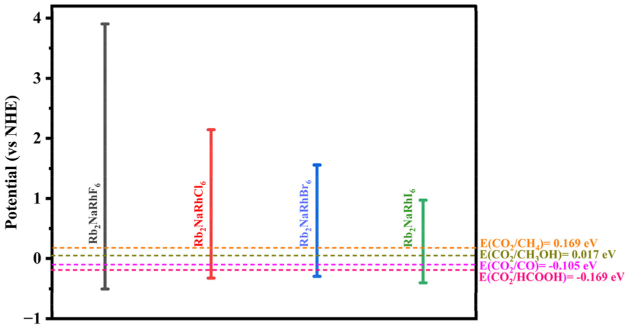

Fig. 11 CO_2 reduction potential of Rb_2NaRhX_6 (X = F, Cl, Br, and I) compounds relative to the normal hydrogen electrode (*vs.* NHE).

5 Photovoltaic application

5.1. Device configuration and modeling parameters

Device configuration and modeling parameters are crucial to calculating because they define the structural, electrical, and optical characteristics of each layer within a simulated device, directly influencing its overall performance.

Table 4 summarizes the input parameters used to simulate the device architecture consisting of FTO/SnS_2/Rb_2NaRhX_6, where X = F, Cl, Br, and I. The table includes the physical, electronic, and transport properties assigned to each layer in the simulation. The thickness of the FTO and SnS_2 layers is fixed at 50 nm, while all four absorber layers, namely Rb_2NaRhF_6, $Rb_2NaRhCl_6$, $Rb_2NaRhBr_6$, and Rb_2NaRhI_6, are taken as 700 nm. This indicates that the halide perovskite-derived layers act as the main absorber region in the device. A clear compositional trend is observed in the band gap (E_g) values. The band gap decreases systematically from 1.819 eV for Rb_2NaRhF_6 to 1.254 eV for Rb_2NaRhC_6, 0.935 eV for $Rb_2NaRhBr_6$, and 0.594 eV for Rb_2NaRhI_6. This reduction from F to I suggests that

Table 4 Configurational parameters for the simulated device architecture

Parameters	FTO	SnS_2	Rb_2NaRhF_6	$Rb_2NaRhCl_6$	$Rb_2NaRhBr_6$	Rb_2NaRhI_6
Thickness (nm)	50	50	700	700	700	700
Band gap, E_g (eV)	3.6	2.24	1.819	1.254	0.935	0.594
Electron affinity, χ (eV)	4.5	4.24	3.239	3.833	4.164	4.521
Dielectric permittivity, ε_r	10	10	2.353	3.696	4.579	6.428
C_B effective density of states, N_C (cm^{-3})	2×10^{18}	2.2×10^{18}	8.43×10^{18}	1.007×10^{19}	1.238×10^{19}	1.247×10^{19}
V_B effective density of states, N_V (cm^{-3})	1.8×10^{19}	1.8×10^{19}	1.512×10^{19}	1.515×10^{19}	1.515×10^{19}	1.503×10^{19}
Donor density, N_D (cm^{-3})	1×10^{18}	1×10^{17}	0	0	0	
Acceptor density, N_A (cm^{-3})	0	0	1×10^{17}	1×10^{17}	1×10^{17}	1×10^{17}
Electron mobility, μ_n ($cm^2\ V^{-1}\ s^{-1}$)	50	50	95	90	90	120
Hole mobility, μ_h ($cm^2\ V^{-1}\ s^{-1}$)	20	50	75	70	70	80
Defect density, N_t (cm^{-3})	1×10^{14}	1×10^{14}	1×10^{14}	1×10^{14}	1×10^{14}	1×10^{14}

replacing the lighter halide with the heavier one progressively narrows the band gap, which is favorable for stronger visible-light absorption.

The electron affinity (χ) also increases from 3.239 eV for Rb_2NaRhF_6 to 4.521 eV for Rb_2NaRhI_6. This means the band edges shift with halide substitution, which can strongly influence band alignment with the transport layers and, therefore, charge extraction efficiency. The dielectric permittivity (ε_r) rises steadily across the series, from 2.353 for the fluoride compound to 6.428 for the iodide compound. This increase implies that the iodide-based material may provide better electrostatic screening and reduced coulombic interaction between charge carriers. The effective density of states in both the conduction band (N_C) and valence band (N_V) remains of the order of 10^{19} cm^{-3} for all absorber layers, with only minor variation. N_C shows a gradual increase from fluoride to iodide, whereas N_V remains nearly constant. This suggests that the four compounds have broadly comparable carrier state availability, with small halide-dependent differences. For the doping profile, FTO and SnS_2 are treated as n-type layers with donor densities of 1×10^{18} cm^{-3} and 1×10^{17} cm^{-3}, respectively. In contrast, the absorber layers are modeled as p-type, each having an acceptor density of 1×10^{17} cm^{-3} and essentially zero donor density. This confirms the intended junction formation between the electron-transport side and the absorber region. The carrier mobility values are relatively high for all absorber materials. The electron mobility varies from 90 to 120 $cm^2\ V^{-1}\ s^{-1}$, while the hole mobility ranges from 70 to 80 $cm^2\ V^{-1}\ s^{-1}$. Among them, Rb_2NaRhI_6 exhibits the highest electron and hole mobilities, suggesting superior charge transport capability compared to the other halide members. Finally, the defect density (N_t) is fixed at 1×10^{14} cm^{-3} for all layers, ensuring a consistent basis for comparison among the simulated devices. In addition to the simulation parameters, the feasibility of experimental fabrication is also considered. The front contact FTO layer is typically deposited at high temperatures (~400–600 °C) using techniques such as spray pyrolysis,[61] which ensures good conductivity and transparency. The SnS_2 electron transport layer can be prepared using chemical bath deposition or sputtering methods at moderate temperatures (~200–400 °C).[62] For the Rb_2NaRhX_6 absorber layer, deposition is expected to occur at relatively lower temperatures (~100–300 °C), depending on the synthesis route, such as solution processing or vacuum-based techniques. The Au back contact is generally deposited by thermal evaporation at room temperature. These temperature ranges indicate that the proposed device architecture is compatible with established thin-film fabrication processes, although experimental validation of Rb-based double perovskite synthesis remains necessary.

5.2. Energy band alignment analysis

Fig. 12 shows the equilibrium energy-band alignment of the FTO/SnS_2/Rb_2NaRhX_6/Au solar-cell structures for four different halide compositions: Fig. 12a Rb_2NaRhF_6, Fig. 12b $Rb_2NaRhCl_6$, Fig. 12c $Rb_2NaRhBr_6$, and Fig. 12d Rb_2NaRhI_6. In each panel, the conduction-band edge (E_C), valence-band edge (E_V), electron quasi-Fermi level (F_n), and hole quasi-Fermi level (F_p) are plotted as a function of device thickness. The absorber layer thickness is kept constant at 0.70 μm, while the SnS_2 and FTO layers are each 0.05 μm thick. A clear halide-dependent reduction in the absorber band gap is observed, decreasing from 1.819 eV for Rb_2NaRhF_6 to 1.254 eV for $Rb_2NaRhCl_6$, 0.935 eV for $Rb_2NaRhBr_6$, and 0.594 eV for Rb_2NaRhI_6. The band profiles remain nearly flat throughout the absorber region, indicating a relatively uniform internal potential, while sharp band offsets appear at the SnS_2/absorber and absorber/FTO interfaces.

5.3. Interface defect parameters

Interfacial defect analysis is essential because defects at the SnS_2/Rb_2NaRhX_6 interface strongly affect charge transport, recombination, and device stability. Parameters such as defect density, defect type, and capture cross-section help identify the trapping behavior of carriers and the recombination activity of the interface states. These defects can significantly reduce photovoltaic performance by lowering V_{OC}, J_{SC}, and PCE. Therefore, this study is important for understanding interface losses and improving solar-cell efficiency through better interface engineering and passivation.

Table 5 presents the interfacial defect parameters used for the SnS_2/Rb_2NaRhX_6 (X = F, Cl, Br, I) heterojunctions in the simulated solar cells. The table shows that the same defect conditions are applied to all four interfaces, allowing a fair comparison of device performance across the halide series. For

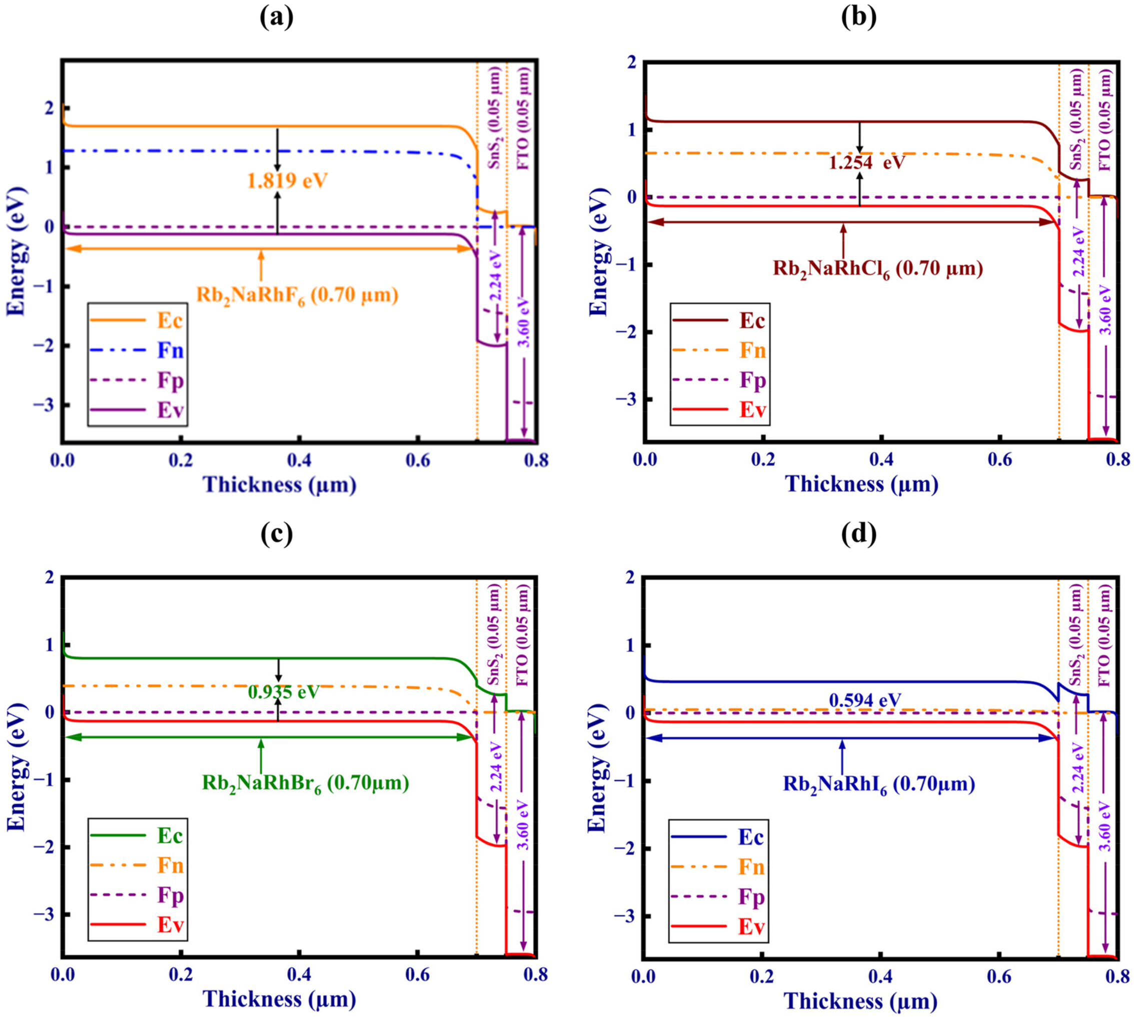

Fig. 12 Effect of X-site halide (X = F, Cl, Br, I) on the energy band diagram of (a) Rb_2NaRhF_6, (b) $Rb_2NaRhCl_6$, (c) $Rb_2NaRhBr_6$, and (d) Rb_2NaRhI_6 double perovskite materials.

each interface, the electron and hole capture cross section is fixed at 1×10^{-19} cm^2, indicating that the defect centers are assumed to have the same carrier trapping probability for both types of charge carriers. The defect type is taken as neutral in all cases, meaning the interfacial trap states are modeled without net charge. In addition, the total defect density is set to 1×10^{11} cm^{-2} for every interface. Because all the interfacial defect parameters remain unchanged for SnS_2/Rb_2NaRhF_6, $SnS_2/Rb_2NaRhCl_6$, $SnS_2/Rb_2NaRhBr_6$, and SnS_2/Rb_2NaRhI_6, any variation in the simulated photovoltaic performance can be attributed mainly to the intrinsic material properties of the absorber layers rather than differences in interface defect assumptions.

Table 5 Comparison of interfacial defect properties in SnS_2/Rb_2NaRhX_6 (X = F, Cl, Br, I) solar cells

Interfaces	Capture cross section: electrons/holes (cm^2)	Defect type	Total defect density (cm^{-2})
SnS_2/Rb_2NaRhF_6	1×10^{-19}	Neutral	1×10^{11}
$SnS_2/Rb_2NaRhCl_6$	1×10^{-19}	Neutral	1×10^{11}
$SnS_2/Rb_2NaRhBr_6$	1×10^{-19}	Neutral	1×10^{11}
SnS_2/Rb_2NaRhI_6	1×10^{-19}	Neutral	1×10^{11}

5.4. Thickness-dependent optimization of photovoltaic performance

Investigating the effect of absorber-layer thickness is essential for optimizing the photovoltaic performance of Rb_2NaRhX_6-based solar cells because it reflects the balance between light absorption, carrier collection, and recombination losses. By changing the thickness systematically, it becomes possible to determine the optimum range where the absorber can harvest sufficient photons while maintaining efficient charge transport. This analysis also explains the evolution of PCE and J_{SC}, which generally improve with thickness up to a saturation point, beyond which further increase gives little benefit and may even enhance bulk recombination and material usage.[63] At the same time, the variation of V_{OC} and FF with thickness provides insight into the electronic quality of the absorber and the stability of the device interfaces. Therefore, thickness-dependent analysis of Rb_2NaRhX_6 absorbers is important not

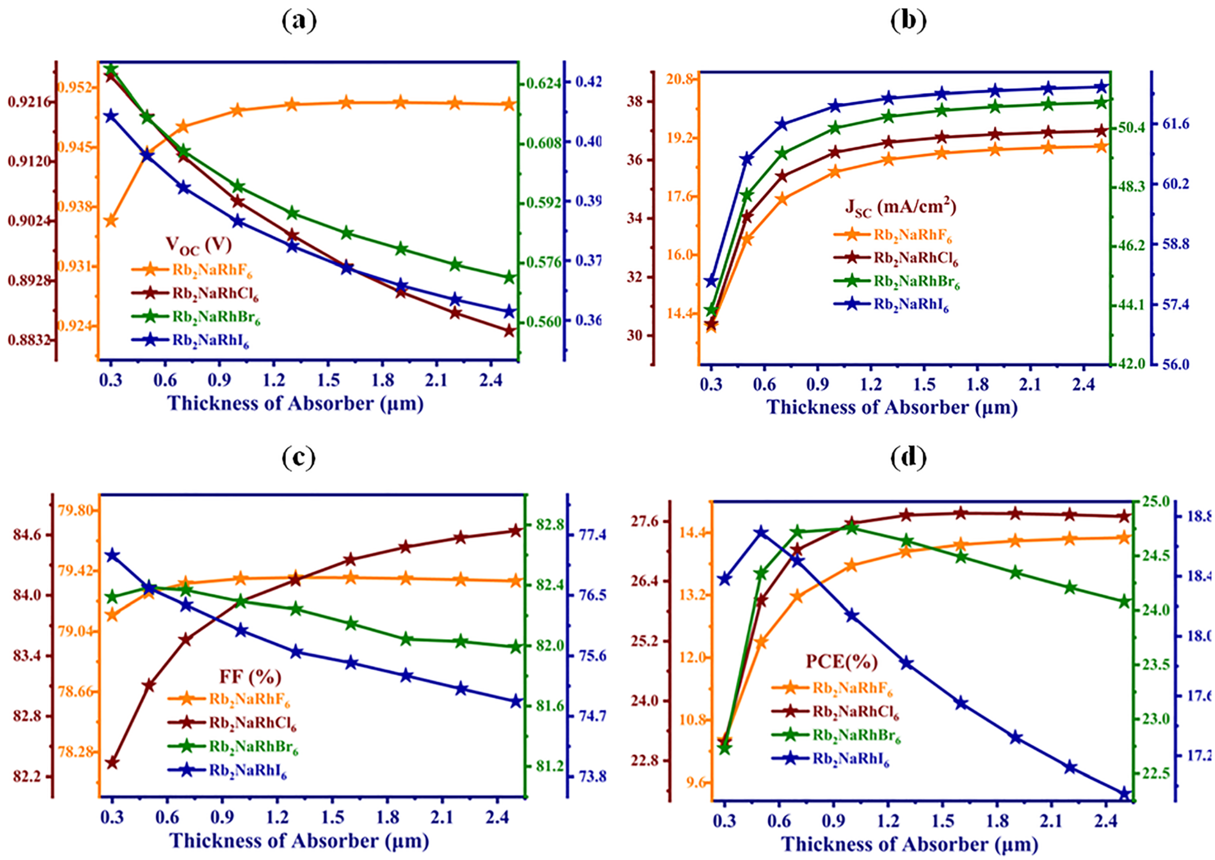

Fig. 13 Variation of (a) V_{OC}, (b) J_{SC}, (c) FF, and (d) PCE with absorber layer thickness for Rb_2NaRhX_6 (X = F, Cl, Br, I)-based solar cells.

only for achieving maximum efficiency with lower fabrication cost, but also for understanding their underlying optoelectronic behavior and practical suitability for photovoltaic applications.

Fig. 13 shows the effect of absorber layer thickness on the photovoltaic parameters of Rb_2NaRhX_6 (X = F, Cl, Br, I)-based solar cells. The absorber thickness varies from about 0.3 to 2.4 µm, and the corresponding changes in V_{OC},J_{SC}, FF, and PCE are presented in Fig. 13a–d. In Fig. 13a, the V_{OC} generally decreases with increasing absorber thickness for all four devices, although the fluoride-based device shows a slight rise at lower thickness and then becomes nearly saturated. The chloride-, bromide- and iodide-based cells exhibit a clearer monotonic decline in V_{OC} as thickness increases. This behavior suggests that a thicker absorber may enhance recombination losses, leading to a reduction in the built-in photovoltage. Moreover, in Fig. 13b, J_{SC} increases rapidly with absorber thickness at the beginning and then approaches saturation for all compounds. This trend is expected because a thicker absorber can capture more incident photons and generate more charge carriers. At lower absorber thicknesses, incomplete photon absorption limits carrier generation despite efficient carrier extraction. As the thickness increases, enhanced light absorption improves J_{SC} and PCE up to an optimum value. Among all devices, Rb_2NaRhI_6 consistently shows the highest J_{SC}, followed by $Rb_2NaRhBr_6$, $Rb_2NaRhCl_6$, and Rb_2NaRhF_6, which is consistent with the narrower band gap of the iodide compound and its stronger light-harvesting ability. Likewise, In Fig. 13c, the FF exhibits different thickness-dependent behavior depending on the halide composition. The fluoride-based device remains nearly constant with only slight variation. The chloride-based solar cell shows a noticeable increase in FF with increasing thickness. In contrast, the bromide- and iodide-based devices display a gradual decrease in FF as the absorber becomes thicker. This indicates that the balance between carrier generation and transport/recombination differs across the halide series. When the absorber thickness exceeds the effective carrier diffusion length, photogenerated carriers require a longer transport path before reaching the electrodes, which increases the probability of bulk recombination and reduces carrier collection efficiency. This effect becomes more pronounced for the bromide- and iodide-based devices at higher thicknesses, where the reductions in V_{OC}, FF, and eventually PCE suggest enhanced recombination losses and shorter effective carrier lifetimes. Similarly, In Fig. 13d, the PCE first increases sharply with increasing thickness and then either saturates or declines slightly, depending on the composition. For Rb_2NaRhF_6 and $Rb_2NaRhCl_6$, the PCE rises and then reaches an almost stable optimum at higher thickness. $Rb_2NaRhBr_6$ reaches its maximum PCE at an intermediate thickness and then slightly decreases. In contrast, Rb_2NaRhI_6 attains its best efficiency at relatively low thickness and then continuously declines as the layer becomes thicker. This indicates that although thicker absorber layers improve light absorption and J_{SC}, excessive thickness can also increase recombination and reduce overall device efficiency, especially for the iodide-based cell. Therefore, the optimized absorber thickness obtained in this work reflects a balance between efficient photon harvesting and effective carrier transport governed by carrier diffusion length, lifetime, and recombination dynamics.

5.5. Influence of doping and defects on the solar cell efficiency

Calculating the effect of defect density and shallow acceptor density is important because it reveals how material quality and doping influence recombination, charge transport, and overall device efficiency. It helps identify defect tolerance limits, the role of doping in enhancing V_{OC} and FF, and guides optimization strategies for achieving stable, high-performance solar cells.[64] In Fig. 14a, increasing the total defect density from 10^{10} to 10^{18} cm^{-3} causes an overall deterioration in device performance for all compositions. The PCE decreases progressively with rising defect density, with the decline being especially pronounced for $Rb_2NaRhBr_6$ and Rb_2NaRhI_6 at higher defect concentrations. $Rb_2NaRhCl_6$ retains the highest efficiency over most of the defect-density range, while Rb_2NaRhF_6 shows the lowest but comparatively stable behavior. The FF also drops with increasing defect density, particularly at defect levels above about 10^{16} to 10^{17} cm^{-3}, indicating enhanced recombination and poorer charge extraction.

The J_{SC} remains almost constant at lower defect densities and then decreases noticeably at higher defect concentrations, especially for the bromide- and iodide-based cells. A similar decreasing trend is observed for V_{OC}, which continuously falls as the defect density increases. This confirms that a high density of defect states acts as recombination centers, reducing both carrier lifetime and overall solar-cell performance.

In Fig. 14b, the effect of shallow acceptor density is quite different. As the shallow acceptor density increases from 10^{13} to 10^{20} cm^{-3}, the PCE of $Rb_2NaRhCl_6$ and $Rb_2NaRhBr_6$ increases steadily, while Rb_2NaRhF_6 remains almost unchanged with only a slight improvement. In contrast, Rb_2NaRhI_6 remains nearly stable at lower acceptor densities but shows a strong decline at higher doping levels. FF follows a similar trend: it improves for the chloride- and bromide-based devices, changes only slightly for the fluoride system, and decreases sharply for the iodide compound at high acceptor concentrations. The J_{SC} is nearly constant for Rb_2NaRhF_6, $Rb_2NaRhCl_6$, and $Rb_2NaRhBr_6$, but drops markedly for Rb_2NaRhI_6 as the acceptor density becomes very high. On the other hand, V_{OC} generally increases with shallow acceptor density for all four compounds, although the increase is much smaller in the iodide-based cell. This suggests that moderate p-type doping improves the built-in potential and junction quality, but excessive acceptor concentration can adversely affect carrier transport and recombination, particularly in Rb_2NaRhI_6.

5.6. Effect of temperature variation

Calculating the temperature-dependent photovoltaic parameters such as PCE, FF, J_{SC}, and V_{OC} is important because the performance and long-term stability of solar cells are strongly influenced by operating conditions, especially thermal effects. Solar cells typically function under outdoor environments where temperature fluctuations are inevitable, and higher temperatures often lead to increased carrier recombination, reduced bandgap, and degraded device efficiency. By analyzing how these parameters vary with temperature, researchers can identify the intrinsic thermal stability of absorber materials,

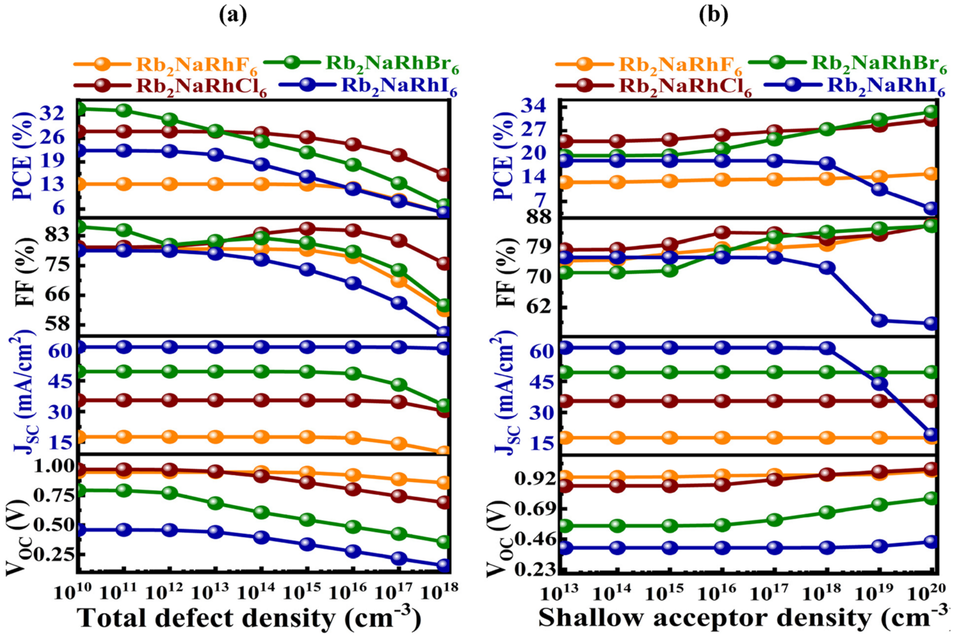

Fig. 14 Variation of photovoltaic parameters of Rb_2NaRhX_6 (X = F, Cl, Br, I) as a function of (a) defect density and (b) shallow acceptor density.

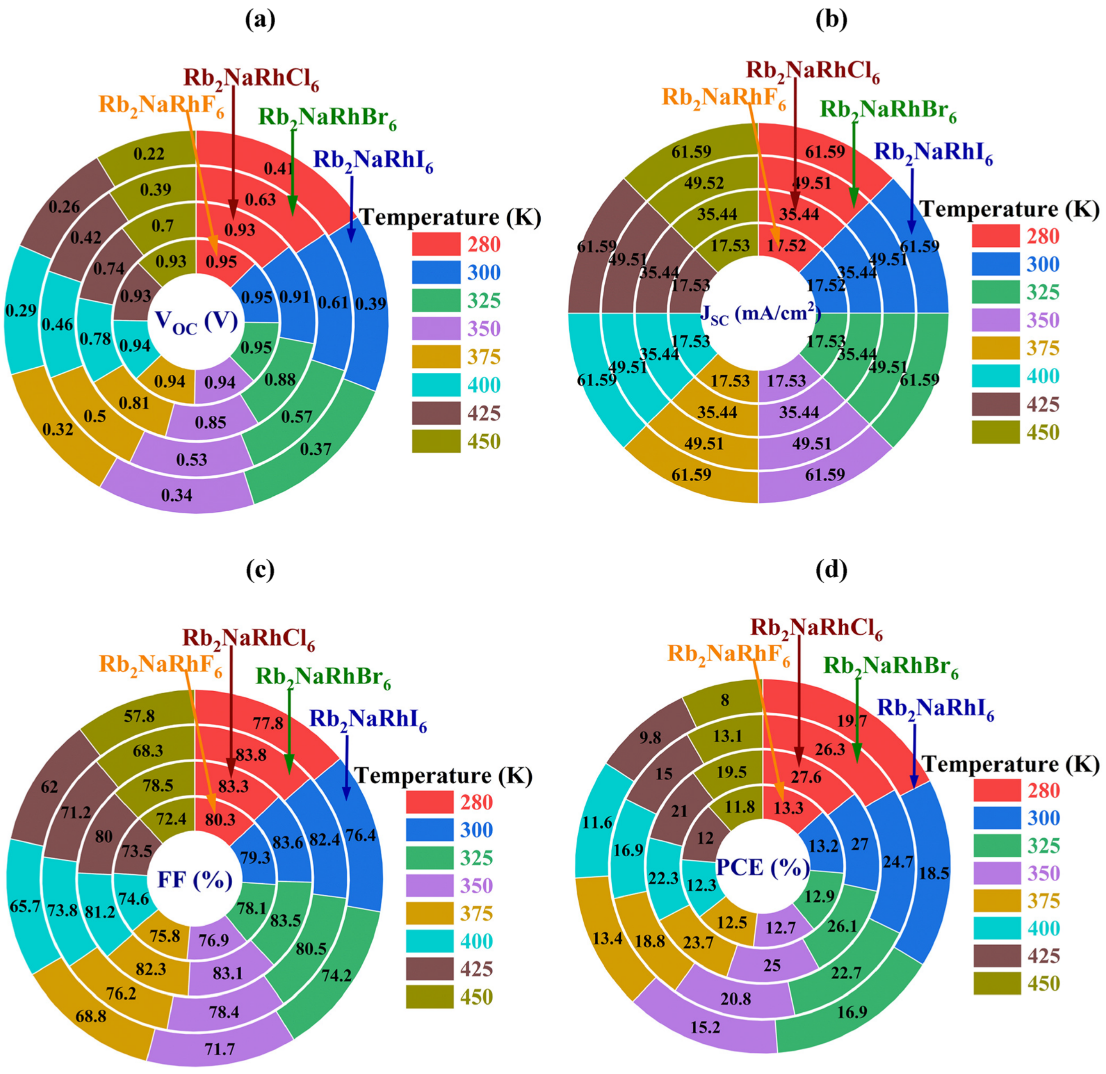

Fig. 15 Temperature-dependent photovoltaic parameters of Rb_2NaRhX_6 (X = F, Cl, Br, I) based solar cells, showing the variation of (a) V_{OC}, (b) J_{SC}, (c) FF, and (d) PCE over the temperature range 280–450 K.

evaluate their suitability for real-world applications, and determine the extent of performance degradation under practical conditions.[65] Specifically, understanding variations in J_{SC} and V_{OC} reveals the carrier generation and transport behavior, while FF and PCE indicate overall device quality and efficiency.

In Fig. 15a, the open-circuit voltage (V_{OC}) generally decreases with increasing temperature for all four devices. At lower temperatures, the value remains relatively high, whereas at elevated temperatures they drop noticeably. This reduction is most significant for the iodide-based cell, while the fluoride- and chloride-based devices retain comparatively higher V_{OC} values over the full temperature range. The gradual loss of V_{OC} with rising temperature is associated with enhanced carrier recombination and thermal broadening effects. In Fig. 15b, the short-circuit current density (J_{SC}) shows the opposite trend and increases steadily with temperature for all compounds. At 280 K, the current density is lowest, and it progressively rises as the temperature reaches 450 K. The highest J_{SC} values are obtained for Rb_2NaRhI_6, followed by $Rb_2NaRhBr_6$, while Rb_2NaRhF_6 and $Rb_2NaRhCl_6$ exhibit comparatively lower current densities. This behavior suggests improved thermal activation of carriers and enhanced carrier collection at higher temperatures.

In Fig. 15c, the fill factor (FF) declines continuously with increasing temperature for each absorber composition. The decrease is relatively modest at first but becomes more noticeable at higher temperatures. Among the four devices, the bromide- and chloride-based cells preserve comparatively higher FF values, whereas the iodide-based system shows a stronger deterioration. This trend reflects the growing influence of resistive losses and recombination as temperature increases. In Fig. 15d, the power conversion efficiency (PCE) decreases overall with increasing temperature for all four solar cells, despite the simultaneous rise in J_{SC}. The temperature-induced reductions in V_{OC} and FF dominate the overall device response and lead to lower efficiency at elevated temperatures. The chloride-based device exhibits the highest PCE throughout most of the temperature range, while the iodide-based device shows the strongest sensitivity to thermal effects and the lowest efficiency at high temperature.

5.7. *JV* and QE

Evaluating the *J*–*V* characteristics and quantum efficiency is important for understanding how effectively a solar-cell material converts light into electrical power. The *J*–*V* analysis provides the main performance indicators, including V_{OC}, J_{SC}, FF, and PCE, and helps identify losses related to recombination and resistance.[66] In contrast, the QE spectrum shows how efficiently incident photons are absorbed and transformed into charge carriers over different wavelengths. Together, these results offer a clear picture of device efficiency, carrier behavior, and spectral response, making them essential for optimizing photovoltaic performance and selecting suitable absorber materials.[66]

In Fig. 16a, the *J*–*V* curves reveal clear differences in photovoltaic performance among the four absorber compositions. The short-circuit current density (J_{SC}) increases systematically from Rb_2NaRhF_6 to Rb_2NaRhI_6, as indicated by the higher current plateau values of the curves. The iodide-based device exhibits the largest current density, followed by the bromide-, chloride-, and fluoride-based devices. This trend reflects the progressive bandgap narrowing from F to I, which allows broader solar absorption and thus greater photocurrent generation. In contrast, the open-circuit voltage (V_{OC}) shows the opposite behavior, with the fluoride- and chloride-based cells maintaining higher voltages, whereas the bromide- and especially iodide-based devices show lower V_{OC}. The rectangularity of the curves also suggests that the fill factor (FF) remains reasonably high, although the iodide system appears to suffer from a lower voltage output despite its strong current response. Overall, the *J*–*V* curves demonstrate the trade-off between voltage and current across the halide series. In Fig. 16b, the QE spectra shows that all four devices possess high photo response over their effective absorption ranges, with QE values remaining close to 100% across much of the spectrum before sharply declining near the absorption edge. The cutoff wavelength shifts markedly toward longer wavelengths from Rb_2NaRhF_6 to Rb_2NaRhI_6. The fluoride-based cell shows absorption only in the shorter wavelength region, while the chloride and bromide compounds extend the response deeper into the visible and near-infrared regions. The iodide-based device exhibits the broadest spectral coverage, extending far into the infrared region, which explains its highest J_{SC}. Thus, the QE spectra confirms that halide substitution strongly tunes the light-harvesting range of the absorber. Taken together, Fig. 13 indicates that moving from F to I broadens the absorption window and significantly enhances current generation, but this improvement is accompanied by a reduction in photovoltage. Therefore, the overall device performance depends on the balance between the higher J_{SC} of the narrow-band-gap absorbers and the higher V_{OC} of the wide-band-gap absorbers.

5.8. Overall photovoltaic performance

It is important to calculate and compare photovoltaic parameters such as PCE, J_{SC}, V_{OC}, and FF because these are the fundamental metrics that determine the real performance and viability of a solar cell material. Each parameter reveals a different aspect of the device such as, J_{SC} reflects the material's ability to generate charge carriers from absorbed photons, V_{OC} indicates the driving force for carrier separation and the quality of the absorber's band alignment, FF measures resistive and recombination losses affecting the overall device quality, and PCE combines all these factors into a single efficiency value. By calculating them, researchers can identify the strengths and weaknesses of different absorber materials, understand the physical processes limiting performance (such as poor absorption, recombination, or instability), and compare candidate materials on a common scale.

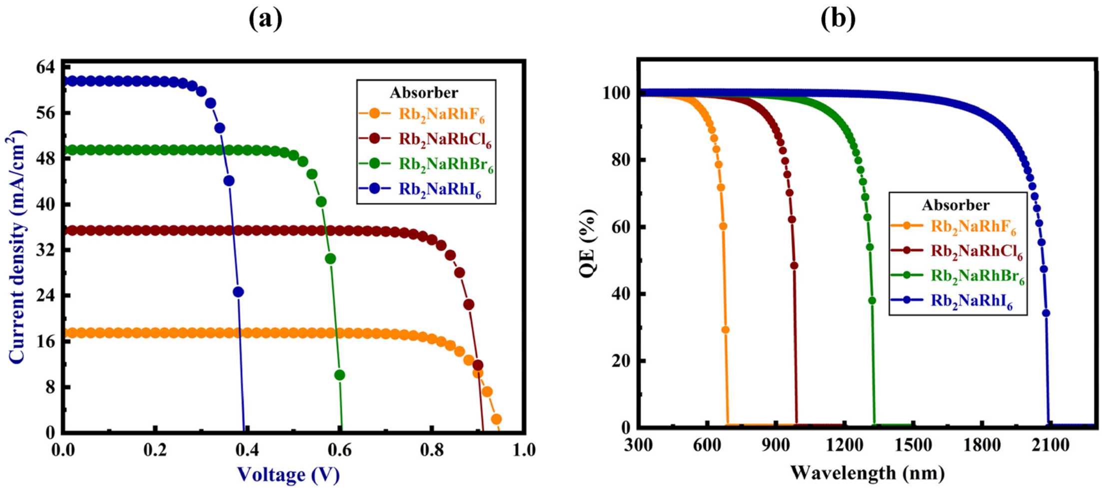

Fig. 16 Simulated photovoltaic characteristics of Rb_2NaRhX_6 (X = F, Cl, Br, I) perovskite solar cells: (a) *J*–*V* curves showing the current density–voltage relationship and corresponding device performance parameters (V_{OC}, J_{SC}, FF, and PCE), and (b) quantum efficiency (QE) spectra as a function of wavelength.

Table 6 Comparative analysis of the calculated photovoltaic parameters of Rb_2NaRhX_6 (X = F, Cl, Br, and I) with previously reported simulation and experimental data

Compound	PCE (%)	J_{SC} (mA cm^{-2})	V_{OC} (V)	FF (%)	Reference
FTO/SnS_2/Rb_2NaRhF_6/Au	13.17	16.57	0.947	79.34	This work
FTO/SnS_2/$Rb_2NaRhCl_6$/Au	27.03	35.41	0.893	83.56	This work
FTO/SnS_2/$Rb_2NaRhBr_6$/Au	24.72	49.79	0.606	82.34	This work
FTO/SnS_2/Rb_2NaRhI_6/Au	18.50	61.59	0.393	76.36	This work
Cs_2NaBiI_6	23.31	21.8	1.23	86.63	Sim.[67]
$Cs_2AgBiBr_6$	23.50	21.38	1.375	79.93	Sim.[68]
$Cs_2AgInBr_6$	26.64	27.49	1.1562	83.79	Sim.[69]
AZO/SnO_2/$MAPbI_3$/D-PBTTT-14/RGO	28.39	28.95	1.13	86.58	Sim.[70]
FTO/SnO_2/perovskite/spiro-OMeTAD/RGO	16.80	22.10	1.10	69.00	Exp.[71]
FTO/SnO_2/perovskite/RGO	24.00	0.99	52.20	12.60	Exp.[71]
FTO/SnO_2/$FAPbI_3$/Spiro/Au	4.3	16.6	40.6	0.6	Exp.[72]
	11.5	20.6	1.1	47.4	Sim.[72]
FTO/SnO_2/$FA_{0.85}Cs_{0.15}PbI_3$/Spiro/Au	9.9	21.4	0.9	51.6	Exp.[72]
	14.5	20.8	1.2	56.9	Sim.[72]
FTO/SnO_2/$FA_{0.85}Cs_{0.15}Pb(I_{0.85}Br_{0.15})_3$/Spiro/Au	15.1	22.6	1.0	64.4	Exp.[72]
	14.7	20.0	1.2	58.2	Sim.[72]

Table 6 presents a comparative analysis of the calculated photovoltaic parameters of Rb_2NaRhX_6 (X = F, Cl, Br, and I) together with previously reported simulation and experimental studies. The comparison demonstrates that the proposed Rb-based double perovskites exhibit highly competitive photovoltaic characteristics relative to several well-known lead-free and Pb-based perovskite systems. For example, the optimized efficiency of $Rb_2NaRhCl_6$ (27.03%) exceeds the simulated efficiencies reported for Cs_2NaBiI_6 (23.31%) and $Cs_2AgBiBr_6$ (23.50%), while remaining highly competitive with $Cs_2AgInBr_6$ (26.64%).

Furthermore, the obtained efficiencies are comparable to or higher than many experimentally fabricated perovskite devices reported in the literature, including FTO/SnO_2/perovskite/spiro-OMeTAD/RGO (16.80%) and FTO/SnO_2/$FA_{0.85}Cs_{0.15}Pb(I_{0.85}Br_{0.15})_3$/Spiro/Au (15.1%). These comparisons strongly support the reliability and practical significance of the present SCAPS-1D simulation results and further justify the relevance of the simulation outcomes to experimentally realizable photovoltaic devices.

Among the four investigated compounds, $Rb_2NaRhCl_6$ exhibits the best overall photovoltaic performance with the highest PCE of 27.03%, achieved through a balanced combination of high J_{SC} (35.41 mA cm^{-2}), V_{OC} (0.893 V), and FF (83.56%). These results indicate efficient charge generation, reduced recombination losses, and effective carrier extraction. $Rb_2NaRhBr_6$ shows the second-highest efficiency of 24.72%, mainly due to its significantly enhanced J_{SC} of 49.79 mA cm^{-2} arising from stronger optical absorption and broader spectral response. However, the reduced V_{OC} of 0.606 V limits its overall efficiency despite maintaining a high FF of 82.34%. Rb_2NaRhI_6 exhibits the highest J_{SC} (61.59 mA cm^{-2}), consistent with its narrow band gap and extended visible-light absorption range. Nevertheless, substantial reductions in V_{OC} (0.393 V) and FF (76.36%) restrict its PCE to 18.50%, suggesting increased recombination and voltage losses. In contrast, Rb_2NaRhF_6 delivers the lowest efficiency of 13.17% due to its wider band gap, which limits light absorption and reduces J_{SC} to 16.57 mA cm^{-2}, although it maintains a comparatively high V_{OC} of 0.947 V. Overall, the results clearly demonstrate the strong influence of halide substitution on the balance between photocurrent generation and photovoltage in Rb-based double perovskite solar cells.

It should be noted that the exceptionally high J_{SC} values predicted for $Rb_2NaRhBr_6$ and Rb_2NaRhI_6 are obtained under optimized simulation conditions in SCAPS-1D and therefore represent the theoretical upper performance limits of these absorber materials. In practical experimental devices, factors such as defect-assisted recombination, interface imperfections, carrier transport losses, parasitic absorption, and non-ideal film morphology may reduce the achievable current density. Nevertheless, the large J_{SC} values obtained in this work are physically reasonable due to the narrow band gaps and strong visible-light absorption characteristics of the bromide- and iodide-based compounds, which enable enhanced photon harvesting over a broad spectral range. Similar trends of high photocurrent generation for narrow-band-gap perovskite absorbers have also been reported in previous simulation and experimental studies. Therefore, although the simulated J_{SC} values may be somewhat higher than those achievable in current experimental devices, the obtained results still provide important theoretical insights and performance limits for future experimental optimization of Rb-based double perovskite solar cells.

Overall, the comparative analysis confirms that the simulated photovoltaic performances of the proposed Rb_2NaRhX_6 compounds are consistent with previously reported simulation and experimental investigations. The excellent performance of $Rb_2NaRhCl_6$, in particular, highlights its strong potential as a promising lead-free absorber material for next-generation high-efficiency perovskite solar cell applications.

6 Conclusion

In this work, the structural, electronic, optical, photocatalytic, and photovoltaic properties of lead-free Rb_2NaRhX_6 (X = F, Cl, Br, I) double halide perovskites were systematically investigated using a combined DFT and SCAPS-1D simulation framework. Structural analysis confirmed that all compounds possess stable cubic phases with negative formation energies, mechanically stable elastic constants, and dynamically stable phonon spectra without imaginary frequencies. The calculated electronic band structures revealed direct band-gap semiconducting behavior, where the band gap systematically decreases from fluoride to iodide compositions because of enhanced Rh-d and halogen-p orbital hybridization. Inclusion of SOC and HSE06 corrections further improved the reliability of the electronic structure calculations. Optical analysis demonstrated strong ultraviolet absorption together with a progressive red shift toward the visible region from F- to I-based compounds. Among the investigated materials, $Rb_2NaRhBr_6$ and Rb_2NaRhI_6 exhibited enhanced visible-light absorption and favorable optical conductivity, indicating strong potential for solar-energy harvesting applications. The calculated dielectric response also increased systematically with heavier halides because of enhanced electronic polarizability. Band-edge alignment analysis showed that Rb_2NaRhF_6, $Rb_2NaRhCl_6$, and $Rb_2NaRhBr_6$ satisfy the thermodynamic requirements for photocatalytic water splitting, with suitable CBM and VBM positions for hydrogen and oxygen evolution reactions. In contrast, Rb_2NaRhI_6 mainly supports hydrogen evolution because of its relatively lower valence-band position. Furthermore, all compounds exhibited favorable conduction-band potentials for photocatalytic CO_2 reduction reactions, indicating their multifunctional photocatalytic capability. The pH-dependent band-edge analysis revealed that the fluoride and chloride systems maintain comparatively stable oxidation and reduction abilities across a broad pH range. The photovoltaic performance evaluated through SCAPS-1D simulations demonstrated that halide substitution strongly influences carrier transport and device efficiency. Among all absorbers, $Rb_2NaRhCl_6$ delivered the best overall photovoltaic response with a maximum PCE of 27.03%, supported by an V_{OC} of 0.893 V, a J_{SC} of 35.41 mA cm^{-2}, and a FF of 83.56%. Overall, the present study establishes Rb_2NaRhX_6 double perovskites as promising lead-free multifunctional materials for photovoltaic devices, photocatalytic hydrogen production, and CO_2 reduction applications, while also providing theoretical guidance for the future design of stable and environmentally friendly perovskite-based energy materials.

Ethical statement

The manuscript's authors agree that there is no research involving human participants, human data or tissue, or animal subjects.

Author contributions

Imtiaz Ahamed Apon, Rifat Rafiu, Md. Azizur Rahman: methodology, validation, software, conceptualization, investigation, formal analysis, data curation, visualization, writing – original draft, and review and editing. Amnah Mohammed Alsuhaibani, Moamen S. Refat, Mohamed Benghanem, S. AlFaify, Noureddine Elboughdiri: investigation, validation, software, formal analysis, data curation, writing – original draft, and review and editing.

Conflicts of interest

The authors have no conflicts of interest.

Data availability

Data will be made available on reasonable request.

Acknowledgements

The researchers wish to extend their sincere gratitude to the Deanship of Scientific Research at the Islamic University of Madinah (KSA) for the support provided to the Post-Publishing Program. Princess Nourah bint Abdulrahman University Researchers Supporting Project number (PNURSP2026R65), Princess Nourah bint Abdulrahman University, Riyadh, Saudi Arabia.

References

1 N. Shah, A. A. Shah, P. K. Leung, S. Khan, K. Sun, X. Zhu and Q. Liao, *Processes*, 2023, **11**(6), DOI: 10.3390/pr11061852.

2 S. Yun, Y. Qin, A. R. Uhl, N. Vlachopoulos, M. Yin, D. Li, X. Han and A. Hagfeldt, *Energy Environ. Sci.*, 2018, **11**, 476–526.

3 T. Kumar, M. Kumar, A. Kumar, R. Kumar and M. Bag, *Energy Fuels*, 2025, **39**, 9185–9231.

4 G. Schileo and G. Grancini, *J. Mater. Chem. C*, 2021, **9**, 67–76.

5 H. Luo, P. Li, J. Ma, L. Han, Y. Zhang and Y. Song, *Adv. Energy Mater.*, 2022, **12**, 2201242.

6 S. Ahmed, M. A. Gondal, A. S. Alzahrani, M. Parvaz, A. Ahmed and S. Hussain, *ACS Appl. Energy Mater.*, 2024, **7**, 1382–1397.

7 Z. Xiao, K.-Z. Du, W. Meng, J. Wang, D. B. Mitzi and Y. Yan, *J. Am. Chem. Soc.*, 2017, **139**, 6054–6057.

8 I. Magaji, A. Shuaibu, M. S. Abubakar and M. Isah, *J. Niger. Soc. Phys. Sci.*, 2021, 334–339.

9 I. Magaji, A. Shuaibu, M. Isah, Y. A. Kauru and A. Hussaini, *Niger. J. Technol.*, 2022, **41**, 854–861.

10 G. A. Nowsherwan, *Discov. Mater.*, 2025, **6**, 15.

11 M. K. Hossain, A. A. Arnab, R. C. Das, K. M. Hossain, M. H. K. Rubel, Md. F. Rahman, H. Bencherif, M. E. Emetere, M. K. A. Mohammed and R. Pandey, *RSC Adv.*, 2022, **12**, 34850–34873.

12 S. Allahyar, S. Allahyar and M. Taheri, *Soc. Sci. Res. Netw.*, 2023, 4341145, DOI: 10.2139/ssrn.4341145.

13 M. S. Uddin, M. K. Hossain, M. B. Uddin, G. F. I. Toki, M. Ouladsmane, M. H. K. Rubel, D. I. Tishkevich, P. Sasikumar, R. Haldhar and R. Pandey, *Adv. Electron. Mater.*, 2024, **10**, 2300751.

14 O. R. Lunge, B. K. Ravidas, S. Bhattarai, R. Pandey, J. Madan, M. K. Roy, M. K. Hossain and D. P. Samajdar, *J. Phys. Chem. Solids*, 2024, **195**, 112260.

15 M. K. Hossain, S. Islam, M. N. Sakib, M. S. Uddin, G. F. I. Toki, M. H. K. Rubel, J. Nasrin, S. H. Shahatha, M. R. Mohammad, A. A. Alothman, C. J. Raorane, R. Haldhar and H. Bencherif, *Adv. Electron. Mater.*, 2025, **11**, 2400348.

16 K. Shivesh, I. Alam, A. K. Kushwaha, M. Kumar and S. V. Singh, *Int. J. Energy Res.*, 2022, **46**, 6045–6064.

17 U. ur Rehman, N. Almousa, K. ul Sahar, A. Ashfaq, K. Mahmood, E. A. Shokralla, M. S. Al-Buriahi, Z. A. Alrowaili, R. Y. Capangpangan and A. C. Alguno, *Energy Technol.*, 2023, **11**, 2300459.

18 B. Rezini, T. Seddik, M. Batouche, H. B. Abdallah, W. Ouerghui, M. M. Salah, M. Ahsan, A. Shaker, T. I. Al-Muhimeed, A. Saeed and M. Mousa, *Physics*, 2025, **7**, 3.

19 A. Aggarwal, M. Raj, A. Narayan, A. Kushwaha and N. Goel, *Phys. Scr.*, 2025, **100**, 085946.

20 S. Porwal, M. Paul, H. Dixit, S. Mishra and T. Singh, *Adv. Theory Simul.*, 2022, **5**, 2200207.

21 A. Amjad, S. Qamar, C. Zhao, K. Fatima, M. Sultan and Z. Akhter, *RSC Adv.*, 2023, **13**, 23211–23222.

22 M. U. N. Tariq, M. Kashif and M. Malik, *J. Opt.*, 2024, DOI: 10.1007/s12596-024-02414-8.

23 H. Sabbah, Z. Abdel Baki, R. Mezher and J. Arayro, *Nanomaterials*, 2023, **14**, 48.

24 K. Neupane, S. Bhattarai, N. Deka, A. S. Alali, A. Yousfi, O. Saidani, Md. F. Rahman, A. Kumar and H. Karamti, *Multiscale Multidiscip. Model. Exp. Des.*, 2025, **8**, 390.

25 M. Raj, M. Pathak, A. Kushwaha and N. Goel, *Phys. Scr.*, 2025, **100**, 075560.

26 L. Dahane and H. Ez-Zahraouy, *Int. J. Hydrogen Energy*, 2025, **145**, 589–600.

27 A. Chinggelkim, L. Kimi, L. Hima, L. Puia, R. Zosiamliana, L. Pachuau, S. Gurung and L. Zuala, *Phys. Scr.*, 2026, **101**, 105922.

28 H. Murtaza, Q. Ain, A. S. Jbara, J. Munir, A. S. Aldwayyan, H. M. Ghaithan, A. A. Ali Ahmed and S. M. H. Qaid, *J. Phys. Chem. Solids*, 2025, **198**, 112427.

29 M. E. A. El Goutni, A. Remil, M. Saidi, M. Batouche and T. Seddik, *Eur. Phys. J. B*, 2025, **98**, 130.

30 K. Sekar, R. Manisekaran, O. M. Nwakanma and M. Babudurai, *Adv. Energy Sustainability Res.*, 2024, **5**, 2400003.

31 S. J. Clark, M. D. Segall, C. J. Pickard, P. J. Hasnip, M. J. Probert, K. Refson and M. C. Payne, *Z. Kristallogr.*, 2005, 567–570.

32 M. D. Segall, P. J. D. Lindan, M. J. Probert, C. J. Pickard, P. J. Hasnip, S. J. Clark and M. C. Payne, *J. Phys.: Condens. Matter*, 2002, **14**, 2717.

33 V. Wilhelm and R. Hoppe, *Z. Anorg. Allg. Chem.*, 1975, **414**, 91–96.

34 Materials Project, https://next-gen.materialsproject.org/materials/mp-14038?formula=Rb2NaRhF6, accessed on May 5, 2026.

35 M. Burgelman, K. Decock, S. Khelifi and A. Abass, *Thin Solid Films*, 2013, **535**, 296–301.

36 H. Mouhib, A. Ait Hssi, Y. Ait Wahmane, L. Atourki, A. Elfanaoui, A. Ihlal and K. Bouabid, *Modell. Simul. Mater. Sci. Eng.*, 2022, **30**, 035011.

37 M. K. Hossain, G. F. I. Toki, A. Kuddus, M. H. K. Rubel, M. M. Hossain, H. Bencherif, Md. F. Rahman, Md. R. Islam and M. Mushtaq, *Sci. Rep.*, 2023, **13**, 2521.

38 J. Huang, D. Zhou, H. Yan, C. Meng, Y. Yang, J. Liu, M. Wang, P. Xu, Z. Peng, J. Chen and G. Li, *J. Mater. Chem. C*, 2024, **12**, 4112–4122.

39 M. K. Hossain, M. H. K. Rubel, G. F. I. Toki, I. Alam, Md. F. Rahman and H. Bencherif, *ACS Omega*, 2022, **7**, 43210–43230.

40 Y. Miyazawa, G. M. Kim, A. Ishii, M. Ikegami, T. Miyasaka, Y. Suzuki, T. Yamamoto, T. Ohshima, S. Kanaya, H. Toyota and K. Hirose, *J. Phys. Chem. C*, 2021, **125**, 13131–13137.

41 T. Ouslimane, L. Et-taya, L. Elmaimouni and A. Benami, *Heliyon*, 2021, **7**, e06379.

42 C. Cercignani, in *The Boltzmann Equation and its Applications*, Springer New York, 1988, vol. 67, pp. 40–103.

43 N. Younes, B. Abdennour and R. El Ouardi, *IUJAS*, 2026, 113–122.

44 W. Khan, R. Charif, R. Makhloufi, A. Terki and M. K. Masood, *Eur. Phys. J. B*, 2025, **98**, 228.

45 M. Achqraoui, N. Bekkioui, H. Jebari and H. Ez-Zahraouy, *J. Phys. Chem. Solids*, 2025, **199**, 112543.

46 L. Dahane and H. Ez-Zahraouy, *Int. J. Hydrogen Energy*, 2025, **145**, 589–600.

47 Y. Selmani, A. Jabar, S. Benyoussef and L. Bahmad, *Int. J. Hydrogen Energy*, 2026, **216**, 153970.

48 T. P. H. Sidiropoulos, N. Di Palo, D. E. Rivas, A. Summers, S. Severino, M. Reduzzi and J. Biegert, *Nat. Commun.*, 2023, **14**, 7407.

49 Md. A. Rahman, R. Rafiu, I. A. Apon, Md. S. Hasan Saikot, I. A. Ovi, N. Elboughdiri, M. Benghanem, S. AlFaify, I. M. Ashraf and H. Albalawi, *Mater. Chem. Phys.*, 2026, **349**, 131777.

50 F. O. Ochedi, D. Liu, J. Yu, A. Hussain and Y. Liu, *Environ. Chem. Lett.*, 2021, **19**, 941–967.

51 M. Yusuf, P. Rosha, F. Qureshi, F. M. Ali and H. Ibrahim, *Sustainable Mater. Technol.*, 2025, **43**, e01332.

52 M. El Akkel and H. Ez-Zahraouy, *Solid State Commun.*, 2024, **394**, 115721.

53 F. A. Nelson, A. Basem, D. J. Jasim, T. E. Gber, M. T. Odey, A. F. Al Asmari and S. Islam, *Int. J. Hydrogen Energy*, 2024, **79**, 1191–1200.

54 M. A. Butler and D. S. Ginley, *J. Electrochem. Soc.*, 1978, **125**, 228–232.

55 X. Ma, B. Lu, D. Li, R. Shi, C. Pan and Y. Zhu, *J. Phys. Chem. C*, 2011, **115**, 4680–4687.

56 Y. I. Kim, S. J. Atherton, E. S. Brigham and T. E. Mallouk, *J. Phys. Chem.*, 1993, **97**, 11802–11810.

57 Y. Xu and M. A. A. Schoonen, *Am. Mineral.*, 2000, **85**, 543–556.

58 I.-C. Man and I. Tranca, *Catal. Today*, 2025, **443**, 114963.

59 Z. Ech-charqy and H. Ez-Zahraouy, *Inorg. Chem. Commun.*, 2025, **177**, 114369.

60 M. El Akkel and H. Ez-Zahraouy, *Solid State Commun.*, 2024, **394**, 115721.

61 E. V. A. Premalal, N. Dematage, S. Kaneko and A. Konno, *Electrochemistry*, 2012, **80**, 624–628.

62 A. K. Singh, A. Almushawwah, M. Bahri, J. D. Major, L. J. Phillips, N. D. Browning and A. J. Hughes, *Energy Technol.*, 2025, **13**, 2500261.

63 F. E. Ikuemonisan, Y. O. Kayode and O. B. Odubote, *Next Mater.*, 2025, **8**, 100870.

64 A. Ikram, U. G. Mustafa, A. Hashibon, M. Wang and H. Anwaw, *Energy AI*, 2026, 100743.

65 A. Mortadi, Y. Tabbai, E. E. Hafidi, H. Nasrellah, E. Chahid, M. Monkade and R. E. Moznine, *Clean Eng. Technol.*, 2025, **24**, 100876.

66 G. G. Njema, B. C. Mosonik, C. C. Ahia and J. K. Kibet, *Chem. – Eur. J.*, 2024, **30**, e202403192.

67 G. A. Nowsherwan, *Opt. Quant. Electron.*, 2025, **58**, 24.

68 M. S. Uddin, M. K. Hossain, M. B. Uddin, G. F. I. Toki, M. Ouladsmane, M. H. K. Rubel, D. I. Tishkevich, P. Sasikumar, R. Haldhar and R. Pandey, *Adv. Electron. Mater.*, 2024, **10**, 2300751.

69 M. Abrar, I. J. Biswas and D. Hodges, *J. Electron. Mater.*, 2025, **54**, 4357–4365.

70 S. Rabhi, K. Sekar, K. Kalna, Y. I. Bouderbala, N. Bouri, N. Oueldna, N. Belbachir, K. Dadda, M. S. Aida and N. Attaf, *Opt. Quant. Electron.*, 2024, **56**, 1372.

71 C. Zhang, S. Liang, W. Liu, F. T. Eickemeyer, X. Cai, K. Zhou, J. Bian, H. Zhu, C. Zhu, N. Wang, Z. Wang, J. Zhang, Y. Wang, J. Hu, H. Ma, C. Xin, S. M. Zakeeruddin, M. Grätzel and Y. Shi, *Nat. Energy*, 2021, **6**, 1154–1163.

72 S. Karthick, S. Velumani and J. Bouclé, *Sol. Energy*, 2020, **205**, 349–357.